

SEARCHING FOR BULK MOTIONS IN THE ICM OF MASSIVE, MERGING CLUSTERS WITH *CHANDRA* CCD DATA

ANG LIU^{1,2}, HENG YU^{1,3}, PAOLO TOZZI^{4,1} AND ZONG-HONG ZHU¹

Draft version December 3, 2024

ABSTRACT

We search for bulk motions in the Intra Cluster Medium (ICM) of massive clusters showing evidence of an ongoing or a recent major merger, with spatially resolved spectroscopy in *Chandra* CCD data. We identify a sample of 6 merging clusters with >150 ks *Chandra* exposure in the redshift range $0.1 < z < 0.3$. By performing X-ray spectral analysis of projected ICM regions selected accordingly to their surface brightness, we obtain the projected redshift maps for all these clusters. After performing a robust analysis of the statistical and systematic uncertainties in the measured X-ray redshift z_X , we check whether the global z_X distribution differs from that expected when the ICM is at rest. We find evidence of significant bulk motions at more than 3σ in A2142 and A115, and less than 2σ in A2034 and A520. Focusing on single regions, we identify significant localized velocity differences in all the merger clusters. We also perform the same analysis on 2 relaxed clusters with no signatures of recent mergers, finding no signs of bulk motions, as expected. Our results indicate that deep *Chandra* CCD data enable us to identify the presence of bulk motions at the level of $v_{BM} > 1000$ km/s in the ICM of massive merging clusters at $0.1 < z < 0.3$. Despite the CCD spectral resolution is not sufficient for a detailed analysis of the ICM dynamics, *Chandra* CCD data constitute a key diagnostic tool complementary to X-ray bolometers onboard future X-ray missions.

Subject headings: galaxies: clusters: intracluster medium — X-rays: galaxies: clusters

1. INTRODUCTION

Clusters of galaxies are the largest virialized systems in the Universe, and the strong interplay between their baryonic and dark components is such that they are at the crossroads between astrophysics and cosmology. It is widely accepted that clusters form in a hierarchical way from a primordial density perturbation field, and evolve through accretion and merging of other virialized halos. In particular, merging between halos frequently happens at early epochs and still occurs today. Such merging processes strongly affect the dynamic structure of clusters, often originating bulk motions in the hot intracluster medium (hereafter ICM). On one hand, ICM bulk motions potentially provide an important diagnostic in the formation and evolution of clusters. On the other hand, the ICM velocity field is extremely difficult to measure with present facilities, and, more important, since the measurements of the cluster properties rely on the assumption of hydrostatic equilibrium, unnoticed bulk motions may significantly affect observables such as total mass proxies and baryon mass fractions (Nagai et al. 2013; Nelson et al. 2014). As a consequence, this will also affects studies of the formation of large scale structure and constraints on cosmological parameters (see Allen et al. 2011, for a review).

The bremsstrahlung emission from the optically-thin, hot ICM is observed in the X-ray band, and it constitutes a powerful diagnostics for the thermodynamics of the ICM itself, allowing one to measure temperature and density of the emitting gas. In addition, thanks to the almost perfect collisional equilibrium, the measurement of the line emission from highly

ionized heavy elements constitutes a direct probe of the metal content of the ICM. Merging processes can introduce several clear signatures in the ICM such as the irregular distribution of the X-ray surface brightness, the inhomogeneous distribution of temperatures, and fluctuations in the ICM velocity field, as already mentioned. These signatures last for one or more dynamical times until the relaxation processes bring the ICM back to hydrostatic equilibrium. The surface brightness distribution and temperature map of the ICM of massive clusters is routinely obtained from X-ray imaging and spatially resolved spectroscopy. The direct observation of bulk motion instead, presents several difficulties. In some rare cases, the bulk motion velocities can be estimated indirectly via the properties of the bow shock resulting from a tangential merging process, as in the well known cases of the Bullet cluster (Markevitch et al. 2002), A2146 (Russell et al. 2011), A520 (Markevitch et al. 2005a), and few others. The turbulence expected as a result of the stirring of the ICM during the merger process can be investigated by the Doppler line broadening in the high resolution spectra obtained with the Reflection Grating Spectrometer onboard of *XMM-Newton*. However, only upper limits in the range 200 – 600 km/s have been obtained, and only for the central regions (Sanders et al. 2010; Pinto et al. 2015). Alternatively, the power spectrum of velocities can be inferred from the power spectrum of gas density fluctuations (Zhuravleva et al. 2014).

A straightforward approach is to directly measure the ICM velocity field along the line of sight through the Doppler shift of its emission lines. The most prominent emission line of the ICM X-ray spectra is the ubiquitous *K*-shell line complex of the H-like and He-like iron at 6.7-6.9 keV rest frame, originally detected by Mitchell et al. (1976). Many other emission lines, including L-shell from iron and α elements transitions, may also be found particularly in the soft energy range (0.5-2.0 keV). However, the *K α* iron complex is the only one which is detectable in any cluster observed with a total number of net counts as low as ~ 1000 in the entire X-ray band (see Yu et al.

¹ Department of Astronomy, Beijing Normal University, Beijing, China 100875; yuheng@bnu.edu.cn, zhuzh@bnu.edu.cn

² Homer L. Dodge Department of Physics and Astronomy, University of Oklahoma, Norman, OK 73019, USA

³ Dipartimento di Fisica, Università di Torino, Via P. Giuria 1, I-10125 Torino, Italy

⁴ INAF - Osservatorio Astrofisico di Arcetri, Largo E. Fermi, I-50122 Firenze, Italy

2011). In fact, iron line emission has been identified in X-ray clusters as distant as $z \sim 1.5$ (Rosati et al. 2004; Stanford et al. 2005; Rosati et al. 2009; Tozzi et al. 2013), though the detection may be challenging at $z > 1.5$ (see, e.g., Tozzi et al. 2015).

Despite this, applying this method to the measurement of ICM bulk motions is extremely challenging. The typical gas velocity of 1000 km/s (Nagai et al. 2003) expected in major mergers, corresponds only to a ~ 20 eV shift of the $K\alpha$ iron line complex at 6.7-6.9 keV rest frame. Such a shift is below the CCD energy resolution of *XMM-Newton*/EPIC, *Chandra*/ACIS and *Suzaku*/XIS (~ 100 eV). This constitutes the major obstacle to the direct measurement of the line-of-sight ICM velocity field. Despite these difficulties, there are a few works that successfully achieved detection of bulk motions in massive, nearby clusters using spatially resolved spectral analysis of CCD data. The first successful detection was made in the Centaurus cluster with *ASCA* (Dupke & Bregman 2001a). The typical bulk motion velocity is constrained to $(2.4 \pm 0.1) \times 10^3$ km/s, and was eventually confirmed by *Chandra* data (Dupke & Bregman 2006). Another case is the Perseus cluster, which is also found to present ICM bulk motions by *ASCA* (Dupke & Bregman 2001b). The first systematic search for ICM bulk motions has been performed by Dupke & Bregman (2005) with *ASCA*, but only 2 out of 12 low redshift ($z < 0.13$) clusters showed reliable signatures of bulk motions. In addition, a significant velocity difference of $(5.9 \pm 1.6) \times 10^3$ km/s between two regions of Abell 576 has been found by combining *Chandra* and *XMM-Newton* data (Dupke et al. 2007).

Thanks to the lower background at high energies, *Suzaku*/XIS has been used to search for radial bulk motions in the ICM through X-ray redshift measurements. However, only upper limits of the order of 2000 km/s are derived for AWM7, Abell 2319 and Coma (Sato et al. 2008; Sugawara et al. 2009; Sato et al. 2011, respectively) and of ~ 300 km/s for the Centaurus (Tamura et al. 2014). Only in one case (Abell 2256, Tamura et al. 2011) a robust detection of a bulk motion of 1500 ± 300 km/s has been found. Recently Ota & Yoshida (2015) searched for gas bulk motion in 8 nearby clusters with *Suzaku*, finding signs of large bulk velocity in excess of their uncertainties only in 2 of them (Abell 2029 and Abell 2255). Despite the low background of *Suzaku*/XIS, its low angular resolution is a major limiting factor for this investigation. Surprisingly, *Chandra* ACIS has not been used often for these studies, despite its high angular resolution which allows one to focus on smaller regions and, in principle, detect more efficiently the effects of bulk motions.

Recently we proposed a strategy to search for bulk motion in the ICM along the line of sight, performing spatially resolved spectral analysis in *Chandra* CCD data of the so called Bullet cluster 1E0657-56 (Liu et al. 2015). This case turned out to be particularly challenging due to the extremely high temperatures, which make the iron emission line complex less prominent, and the fact that the merger is occurring in the plane of the sky. Nevertheless, we were able to find a tantalizing $\sim 2\sigma$ evidence for bulk motion of significant mass of ICM in two regions near the center. This is consistent with a picture where the ICM is pushed perpendicularly to the bullet trail due to the extremely large pressure reached when crossing the main cluster center. Future missions carrying X-ray bolometers (e.g. Astro-H, Takahashi et al. 2014) may be able to confirm or rule out this result (see the recent simulations by Biffi et al. 2013).

In this work, we intend to apply our technique to a sample of massive, merging clusters imaged by *Chandra*. Our goal is to investigate whether ICM bulk motions in medium redshift ($z \sim 0.1-0.3$) clusters classified as major mergers, can be detected in *Chandra* ACIS data. We also try to provide robust estimators of the ICM bulk motions whenever possible, like the global *rms* velocity difference across the cluster v_{BM} and the maximum velocity difference measured across the cluster Δv_{max} . We also aim at providing a qualitative description of the dynamical status of the ICM in single clusters by visual inspection of the redshift map, to exploit the angular resolution of *Chandra*.

The Paper is organized as follows. In Section 2, we describe the sample selection. In Section 3, we describe the X-ray data reduction and analysis, including a brief description of the strategy already presented in (Liu et al. 2015). In Section 4, we present results for the single clusters, while in Section 5 we synthesize the results for the entire sample. In Section 6 we discuss future prospects for improvements in this field. Finally, in Section 7 we summarize our conclusions. Throughout this paper, we adopt the 7-years WMAP cosmology, with $\Omega_m = 0.272$, $\Omega_\Lambda = 0.728$ and $H_0 = 70.4$ km s $^{-1}$ Mpc $^{-1}$ (Komatsu et al. 2011). Quoted error bars always correspond to 1σ confidence level.

2. SAMPLE SELECTION

We search in the *Chandra* data archive for clusters classified as merger, on the basis of their X-ray morphology, radio diffuse emission, and/or galaxy dynamics, in the redshift range $0.1 < z < 0.3$. Since our goal is to perform spatially resolved spectral analysis with high signal-to-noise ratio (S/N), we require long exposure times. We fix the threshold for the minimum total exposure to 150 ks on ACIS-I or ACIS-S. The signatures of an occurring, or impending, major merger, are a clear bimodal or multiple structure in the redshift distribution of the member galaxies, strongly disturbed appearance in the X-ray surface brightness, or the presence of a radio halo or radio relic. We found 6 clusters showing at least one of these prominent properties. The clusters are listed in Table 1 in order of increasing optical redshift, together with *Chandra* Obsid and total exposure time (after data reduction).

A2142 is classified as a merger on the basis of the X-ray morphology (Parekh et al. 2015) and the presence of a radio halo (Cuciti et al. 2015). A2034 is classified as a merger on the basis of a shock visible in the X-ray surface brightness (Owers et al. 2014). Abell 115 has a clear bimodal appearance in the X-ray and has a radio relic (Cuciti et al. 2015). A520 shows a clear radio halo (Cuciti et al. 2015) and a clearly disturbed appearance in the X-ray band. 1RXSJ0603.3+4214 has a clear bimodal structure and bright, peculiar radio relic, known as the “Toothbrush” (van Weeren et al. 2012). A2146 shows a prominent bow shock in *Chandra* X-ray image, indicating a violent merger analogous to the more famous Bullet cluster 1E0657-56 which was the subject of our first investigation of ICM bulk motion (Liu et al. 2015). The properties of each cluster will be discussed in more details in Section 4.

As an immediate check of the robustness of our analysis, we also select 2 relaxed clusters in the same redshift range and with comparable exposure depth. The 2 clusters in this control sample are Abell 1689 and Abell 1835, and are listed in Table 2. Clearly, we do not expect to detect any departure from statistical noise in the z_X distribution of these relaxed clusters.

TABLE 1

SAMPLE OF MERGING CLUSTERS AND CORRESPONDING *Chandra* OBSERVATIONS USED IN THIS WORK. THE OBSERVING MODE IS VFaint FOR ALL THE ObsID. THE EXPOSURE TIMES IN THE 4TH COLUMN CORRESPOND TO THE EFFECTIVE VALUES AFTER DATA REDUCTION. OPTICAL REDSHIFT REFERENCES: 1=[PAREKH ET AL. \(2015\)](#); 2=[MURIEL & COENDA \(2014\)](#); 3=[HIROI ET AL. \(2013\)](#); 4=[CASSANO ET AL. \(2013\)](#); 5=[VAN WEEREN ET AL. \(2012\)](#); 6=[PIFFARETTI ET AL. \(2011\)](#).

| Cluster name | Optical redshift | ObsID | Total exposure (ks) |
|---------------|--------------------|---|---------------------|
| A2142 | 0.090 ¹ | ACIS-S: 15186-16564-16565 | 155.1 |
| A2034 | 0.113 ² | ACIS-I: 7695-2204-12885 13192-12886-13193 | 254.5 |
| A115 | 0.197 ³ | ACIS-I: 13458-13459-15578-15581 | 310.6 |
| A520 | 0.203 ⁴ | ACIS-I: 4215-9424-9425-9426-9430 | 516.4 |
| 1RXSJ060313.4 | 0.225 ⁵ | ACIS-I: 15171-15172-15323 | 235.9 |
| A2146 | 0.234 ⁶ | ACIS-I : 12245-12246-12247-13020 13021-13023-13120-13138 | 375.3 |

TABLE 2

RELAXED CLUSTERS AND CORRESPONDING *Chandra* OBSERVATIONS USED IN THIS WORK. THE OBSERVING MODE IS VFaint FOR ALL THE ObsID. THE EXPOSURE TIMES IN THE 4TH COLUMN CORRESPOND TO THE EFFECTIVE VALUES AFTER DATA REDUCTION. OPTICAL REDSHIFT REFERENCE: 7=[HIROI ET AL. \(2013\)](#); 8=[GIRARDI ET AL. \(2014\)](#)

| Cluster name | Optical redshift | ObsID | Total exposure (ks) |
|--------------|--------------------|-----------------------------|---------------------|
| A1689 | 0.183 ⁷ | ACIS-I: 5004-6930-7289-7701 | 151.3 |
| A1835 | 0.252 ⁸ | ACIS-I: 6880-6881-7370 | 193.7 |

3. DATA REDUCTION AND ANALYSIS

3.1. Data reduction

The *Chandra* observations used in this work are listed in Table 1 and 2. All the observations are taken in VFaint mode with ACIS-I, except in the case of A2142 which was observed with ACIS-S. The data are reduced using the *ciao* software (version 4.7) with CALDB 4.6.8. The detailed procedure of data reduction has been described in [Liu et al. \(2015\)](#). The area of the clusters used in this analysis is defined as the circular region which provides the maximum S/N in the 0.5-10 keV band, once the unresolved sources are removed. Point sources are detected by running the *wavdetect* task and then visually inspected, in particular to remove those deeply embedded in the strong ICM emission. The background files are extracted from a series of circular regions as far as possible from the cluster area, but still on the solid angle defined by the overlap of all of the ObsIDs. To define the cluster subregions we apply the contour binning technique ([Sanders 2006](#)) within the maximum S/N circle. Regions are identified simply on the basis of the surface brightness contours in the 0.5-10 keV band image. To make sure that each region can be used to constrain the X-ray redshift with comparable accuracy, we set a criterion in terms of S/N in the 0.5-10 keV band on each region. Clearly this criterion does not take into account the expected gradient in the iron abundance which significantly affects the visibility of the iron emission line complex. We set this threshold to $S/N > 140$, except in the case of Abell 2146 where we choose a weaker constraint $S/N > 100$, due to the relatively lower number of counts. The S/N threshold and the number of regions selected in each cluster are listed in Table 3. For each region the spectrum is extracted from the merged event file after removal of unresolved sources, while calibration files (response matrix files, RMF, and ancillary response files, ARF) are generated independently for each ObsID and then combined by weighting them by the corresponding exposure times. In this way we keep track of all the differences in the ACIS effective area among different regions in the de-

TABLE 3

THE MINIMUM S/N REQUIRED IN EACH REGION AND THE NUMBER OF REGIONS SELECTED FOR SPECTRAL ANALYSIS IN EACH CLUSTER.

| Cluster name | minimum S/N (0.5-10 keV) | number of regions |
|-----------------|-----------------------------|-------------------|
| A2142 | 140 | 52 |
| A2034 | 140 | 14 |
| A115 | 140 | 18 |
| A520 | 140 | 20 |
| 1RXSJ060.3+4214 | 140 | 9 |
| A2146 | 100 | 19 |
| A1689 | 140 | 10 |
| A1835 | 140 | 11 |

tector and among ObsIDs taken at different epochs.

3.2. Spectral analysis

In this work we use the same analysis strategy presented in [Liu et al. \(2015\)](#) to measure the projected X-ray redshift z_X in each region and estimate the total (statistical and systematic) uncertainty. Our analysis is optimized on the basis of spectral simulations shown in [Liu et al. \(2015\)](#). Here we simply recall the relevant aspects of the adopted spectral analysis.

The spectra are analysed using *Xspec* v12.8.2 ([Arnaud 1996](#)). To successfully model the X-ray emission, we use two *mekal* plasma emission models ([Mewe et al. 1985, 1986](#); [Kaastra 1992](#); [Liedahl et al. 1995](#)) which include thermal bremsstrahlung and line emission, with abundances measured relative to the solar values of [Asplund et al. \(2005\)](#) in which $Fe/H = 3.6 \times 10^{-5}$. During the fit, the redshift parameters of the two thermal components are always linked together, while the two temperatures and abundances are left as free parameters.

The main advantage in using a double-temperature thermal spectrum is reducing the possible bias in the measurement of the iron line centroid due to the presence of unnoticed thermal structure along the line of sight. As a matter of fact, different temperature components above 3 keV are not detectable, and a single-temperature thermal component would

return an excellent fit even in the presence of widely different temperatures (see [Mazzotta et al. 2004](#)). However, in [Liu et al. \(2015\)](#) we showed with spectral simulations that the use of two components provide better results for the measurement of the actual redshift of the ICM, while the temperature structure, which is not our main interest here, is left essentially unconstrained. Clearly, this also introduce a larger systematic uncertainty associated to the temperature structure, which is carefully evaluated during our analysis, as explained below.

The Galactic absorption is described by the model `tbabs` ([Wilms et al. 2000](#)). The central value of Galactic HI column density $N_{\text{H,Gal}}$ are based on [Kalberla et al. \(2005\)](#). We conservatively allow $N_{\text{H,Gal}}$ to vary by an interval of $\sim 10\%$ around the central value. This has a small effects since our best-fit z_X are obtained from spectral fits in the hard (2-10 keV) band, which is only marginally affected by the Galactic absorption. Cash statistics ([Cash 1979](#)) is applied to the unbinned source plus background spectra in order to exploit the full spectral resolution of the ACIS-I and ACIS-S CCD. Cash statistics is preferred for faint spectra with respect to the canonical χ^2 analysis of binned data ([Nousek & Shue 1989](#)). To avoid local minima we repeat the fit several times before and after running the `steppar` command on all the free parameters and particularly on the redshift, with a step $\delta z = 10^{-4}$. Finally, the plots of ΔC_{stat} versus redshift are visually inspected to investigate whether there are other possible minima around the best-fit values (see also [Yu et al. 2011](#)), which may indicate a noisy spectrum and therefore an unreliable best-fit value for z_X . We decide to conservatively exclude all the results with a secondary minimum closer than $\Delta C = 6.6$, which corresponds to a formal 99% confidence level for one free parameter.

Our reference spectral analysis consists of two steps. As the first step, we fit the spectra in the 2.0-10 keV energy range to obtain the best fit redshift. We choose to use only the 2-10 keV energy range to minimize the effects of the presence of low temperature components on the centroid of the iron line emission complex. This conservative choice is also supported by the spectral simulations we presented in [Liu et al. \(2015\)](#). For each region, we produce a plot showing the ΔC_{stat} value versus the redshift, obtained by varying redshift parameter and marginalizing the fit with respect to the other parameters. The minimum is generally well defined and roughly symmetric, therefore provides a robust estimate of the statistical uncertainty.

As a second step, we carefully take into account systematic uncertainties on redshift due to the unknown thermal structure of the ICM. We conservatively consider all the possible temperature distributions of the ICM by setting a four-dimensional grid of spectral parameters, namely temperature and abundance of the two thermal components T_1 , T_2 , Z_1 , and Z_2 . The steps of the grid are typically 0.5 keV for the temperature and 0.05 for the metal abundance. Clearly, only a subgrid of temperature and abundance values should be taken into account, since some combination of them provide unacceptable fit. To efficiently select the subgrid, we make use of the full, 0.5-10 keV energy range, in order to exploit the complete information on the thermal structure and the chemical composition. Therefore, for each region, we measure the best fit redshift in the full, 0.5-10 keV band leaving all the parameters free, and collect the absolute minimum C_{min} . Then, we select all the sets of values on the grid which provide a best fit close enough to the absolute best fit. The criterion we adopt is given by $\Delta C_{\text{stat}} \equiv C_{\text{stat}} - C_{\text{min}} < 4.72$, which corresponds to 1σ confidence level for four free parameters.

By applying the criterion $\Delta C_{\text{stat}} < 4.72$ for the fits performed in the full 0.5-10 keV band, we select the subgrid of T_1 , T_2 , Z_1 and Z_2 values statistically compatible within 1σ with the spectrum observed in each region. Then, we run the spectral fit on the subgrid but focusing again in the 2.0-10 keV band only, and measure a set of best-fit z_X values corresponding to the subgrid parameters. The distribution of z_X obtained in this way is used to derive a redshift range defined by the upper and lower 90% percentiles of the z_X distribution on the grid, and thus the systematic uncertainties on redshift. Since the systematic uncertainty σ_{syst} is due to the degeneracy of the temperature values, we assume that it is uncorrelated to the statistical error σ_{stat} . Therefore, we compute the total 1σ un-

certainty as $\sigma_{\text{tot}} = \sqrt{\sigma_{\text{stat}}^2 + \sigma_{\text{syst}}^2}$. We do not consider other relevant sources of systematic errors. Systematics related to calibration issues or time dependence of the gain are kept under control with a direct check on the fluorescent lines of Au L_α and Ni K_α , which are prominent in the ACIS-I background spectrum at 7.5 and 9.7 keV, respectively. Typically, uncertainties introduced by calibration variation (as a function of position on the CCD or as a function of the observation period) on the merged spectrum of each region correspond to errors ~ 5 times smaller than the typical total uncertainty on z_X (see [Liu et al. 2015](#)). Having assessed that gain-calibration does not significantly affect our conclusions, we do not perform a full treatment of the gain-calibration uncertainties in ACIS-I data.

The complete spectral results for each clusters can be found in the appendix, where the best-fit redshifts and the corresponding lower and upper, statistic and systematic error bars are listed for each region of each cluster (values are rounded to the fourth decimal digit). Results are presented in the form of redshift maps and significance maps. In particular, in the significance maps we combine the information included in the best-fit redshift and the corresponding total error by showing $(z_X - \langle z_X \rangle) / \sigma_{\text{tot}}$, where $\langle z_X \rangle$ is the average z_X found across the analyzed regions for which we have reliable spectral fit. Significant (larger than 2σ) deviations in the redshift map are thus visible as bright-blue and bright-red regions.

3.3. ICM dynamical analysis

In this Section we describe how we use the results of the spatially resolved spectral analysis to investigate and possibly characterize the presence of bulk motions in the ICM of each cluster. The first check, analogous to what we did in [Liu et al. \(2015\)](#), is to perform a simple χ^2 test on the distribution of z_X under the assumption of a unique value for the ICM redshift. Therefore we compute $\chi^2 \equiv \sum (z_X - \langle z_X \rangle)^2 / \sigma_{\text{tot}}^2$ and, assuming $N_{\text{reg}} - 1$ degrees of freedom, where N_{reg} is the number of selected regions, we evaluate the probability of being inconsistent with the constant redshift hypothesis. To account for the small differences in the lower and upper error bars, we use the corresponding total error for z_X values lower or higher than $\langle z_X \rangle$.

We also compute the typical bulk motion velocity as the excess of the redshift fluctuations with respect to the statistical and systematic noise. To do that, we simply compute the total root mean square deviation of z_X with respect to the mean, defined as $\sigma_{\text{rms}}^2 \equiv \sum (z_X - \langle z_X \rangle)^2$, and compare it to the average uncertainty $\langle \sigma_{\text{tot}} \rangle = \sum \sigma_{\text{tot}} / N_{\text{reg}}$ (where we use the average value of the lower and upper error bar when they differ). The average excess, which can be ascribed to bulk motions, is computed as $\sigma_{\text{BM}}^2 = \sigma_{\text{rms}}^2 - \langle \sigma_{\text{tot}}^2 \rangle$. Therefore, the bulk motion

velocity averaged over the region included in the maximum S/N radius is finally estimated as $v_{\text{BM}} = c \times \sigma_{\text{BM}} / (1 + \langle z \rangle)$. The error on v_{BM} is estimated as $\sqrt{2}$ times the total error on the mean. Moreover, in those cases where there is some evidence of bulk motions in the ICM, we also provide the value of the maximum velocity difference Δv_{max} found across all the regions with reliable spectral fit.

We visually inspect the histogram distribution of z_{X} and the redshift and significance maps to infer information on the dynamical status of the ICM. This has been done in Liu et al. (2015) for the Bullet cluster, where the two regions with a maximally different redshift are found to be aligned along the bullet trail. We tentatively interpreted them as two regions pushed in opposite directions and perpendicularly to the direction of the bullet at velocities $\sim 5 - 6 \times 10^3$ km/s with respect to the average cluster redshift. Clearly, it is not always possible to draw simple pictures like this one. However, we try to achieve a simple qualitative classification as pre-merger, ongoing or post-merger, according to whether we can clearly identify two well-defined halos with distinct redshift or a few scattered regions with different redshift. Along the same line, clusters with disturbed surface brightness but no signs of bulk motion, may be described as post-merger, a phase in which the bulk motions created by the merger already evolved towards a turbulent velocity field with velocity values below the sensitivity achievable in our data. As previously discussed, the regime of evolved merger, when most of the initial kinetic energy due to the merger evolved into a turbulent velocity field of few $\times 100$ km/s, can be probed only with the much higher spectral resolution of X-ray bolometers.

4. RESULTS ON INDIVIDUAL CLUSTERS

In this section we show the results of our analysis. For each of the clusters, we measure the best-fit redshift in all of the selected regions, and hence obtain the redshift map and the significance map as defined in Section 3.2. We also measure the global redshift z_{Xtot} , which is defined as the best-fit redshift of the total emission of the cluster within the maximum S/N circle. This value corresponds to the emission-weighted average redshift of the ICM, which in principle may differ significantly from the simple average redshift among the regions $\langle z \rangle$. The statistical significance of the presence of bulk motions is evaluated in each case. Whenever possible, we estimate the typical velocity of the bulk motion v_{BM} and the maximum velocity difference Δv_{max} . Moreover, for each cluster we provide a short summary of the available literature concerning their dynamical status.

4.1. Abell 2142

Abell 2142 has been identified as a merger cluster already on the basis of ROSAT observations (Henry & Briel 1996), and more recently has been classified as “non-relaxed” on the basis of the X-ray morphology with Chandra data by Parekh et al. (2015). The two cold fronts, identified in the northwest and southeast regions, clearly separate cooler ($kT \sim 7 - 9$ keV) from hotter ($kT > 12$ keV) gas (Markevitch et al. 2000), making it a promising target to investigate the onset of Kelvin-Helmholtz instabilities at the cold fronts. Evidence of dynamical substructure was also found with optical spectroscopy of the member galaxies (Oegerle et al. 1995). Interestingly, the presence of a narrow-angle tailed radio galaxy may be explained by significant bulk motions in the ICM, as suggested by the statistical analysis of Bliton et al. (1998). Finally,

A2142 has been reported to have a radio halo in Cuciti et al. (2015).

We use the three most recent observation with Chandra ACIS-S for a total of 155.1 ks, as listed in Table 1, while we discard two older observations with ACIS-I (ObsID 5005 and 7692). This choice will minimize the difference of calibration between ObsID. The total number of net counts in the 0.5-10 keV band within a circle of 3 arcmin is about 10^6 in the merged 0.5-10 keV image. This makes A2142 an ideal target for our analysis, with 52 regions potentially useful for spatially resolved spectral analysis. The best fit redshift obtained fitting the total X-ray emission within 3 arcmin is $z_{\text{Xtot}} = 0.0852^{+0.0012}_{-0.0009}$. To evaluate the systematic uncertainty on z_{X} we consider a temperature range from 3 to 16 keV to explore the temperature structure of the ICM, despite the projected temperature shows only a moderate range from 8 to 12 keV. Metal abundances are mildly scattered around $Z = 0.45Z_{\odot}$ in units of Asplund et al. (2005), nevertheless we consider a wide range $0.15 < Z/Z_{\odot} < 1.5$ in order to account for possible large fluctuations.

We find that in 5 regions the X-ray spectral analysis does not provide a reliable value of z_{X} , therefore we use only 47 regions. The best-fit z_{X} of the regions used in our analysis with the corresponding statistical and systematic errors are listed in Table 5. The average redshift is $\langle z_{\text{X}} \rangle = 0.0855$, which is almost coincident with the global, emission-weighted redshift z_{Xtot} .

The hypothesis of a constant redshift is rejected at more than 3σ , with a $\chi^2 = 88.02$ for 46 degrees of freedom, as listed in Table 4. However, the histogram distribution of z_{X} (see Figure 1) clearly shows that the evidence of bulk motions comes from three regions (region 2, 8 and 50) maximally distant from the average redshift. The rest of the z_{X} values is distributed according to a Gaussian slightly narrower than the Gaussian whose variance is the average σ_{tot}^2 . This is expected since we assumed a very conservative estimate for σ_{tot} . The projected X-ray redshift map and significance map are shown in Figure 2. We measure $v_{\text{BM}} = 1400 \pm 300$ km/s for the average bulk motion velocity in the ICM of A2142 within a radius of 3 arcmin. Excluding the three extreme z_{X} regions, we are able to put a hard upper limit of $v_{\text{BM}} < 1450$ km/s. This result is consistent with the Suzaku X-ray spectral analysis by Ota & Yoshida (2015) which provided $\Delta v < 4200$ km/s. However, thanks to the Chandra angular resolution, we find that region 50 is redshifted with respect to the average velocity by 5000 ± 1500 km/s, while the contiguous regions 2 and 8 are blueshifted by 7400 ± 2200 km/s. In particular, we can interpret region 50 as being dominated by a significant amount of ICM mass pushed at high velocity as a result of the ongoing merger. The blueshifted two regions, can be tentatively associated to some rotation of the ICM. We remark that, given the small field of view of the ACIS-S detector, we repeated the spectral analysis with a different choice of the background, finding the same statistical results. Therefore our conclusions are not affected by uncertainties in the background, despite the cluster emission covers almost the entire ACIS-S field of view.

To summarize, as in the case of the Bullet cluster (Liu et al. 2015), the evidence of bulk motions is coming from few regions with extreme redshift difference with respect to the mean, after a very conservative selection of reliable spectra and accurate estimate of the total uncertainty on z_{X} . This may suggest that the cluster is a post merger, or caught in a stage where the shocks are developed since ~ 1 dynamical time or

more and the velocity field of the ICM still shows a few regions with large velocities with respect to the velocity of the center of mass. The interpretation in terms of ICM dynamics is nevertheless still very hard, and a significantly higher spectral resolution with the same angular resolution is needed before the actual velocity field of the ICM can be accurately measured.

4.2. Abell 2034

Abell 2034, at redshift $z_{\text{opt}} = 0.113$ (Muriel & Coenda 2014), shows many signatures typically associated to merging clusters, from radio relic near the position of a discontinuity in the X-ray surface brightness, to significant heating of the ICM above its equilibrium temperature, and significant offset of the cD galaxy from the centroid of the X-ray emission (Kempner & Sarazin 2001; Kempner et al. 2003; Giovannini et al. 2009; van Weeren et al. 2011). In a recent detailed study by Owers et al. (2014) using a deep *Chandra* observation of 250 ks, a shock with a Mach number of 1.59 ± 0.06 , corresponding to a shock velocity of ~ 2000 km/s, was clearly observed. Combining *Chandra* data with spectroscopic observations for 328 spectroscopically confirmed member galaxies, they show the presence of a substructure located at the front edge of the shock and that the merger is proceeding along a north-south direction with an inclination angle of $\sim 23^\circ$ with respect to the plane of the sky. The cluster is included in the sample of the Merging Cluster Collaboration sample⁵.

We use *Chandra* ACIS-I observations for a total of 254.5 ks. The total number of net counts in the 0.5-10 keV band is 2.66×10^5 within a circle of 3 arcmin in the merged image. We select 14 ICM regions for redshift analysis, but we obtained reliable spectral fit only in 11 out of 14. We find $z_{\text{Xtot}} = 0.1124^{+0.0039}_{-0.0044}$ in very good agreement with z_{opt} and $\langle z_{\text{X}} \rangle = 0.1122$. To evaluate systematic uncertainties on z_{X} we consider a temperature and abundance range of 6-12 keV and 0.2-0.8 Z_{\odot} , respectively. The best-fit z_{X} of the 11 regions used in our analysis with corresponding errors are listed in Table 6. The histogram distribution of z_{X} shows that most of the best-fit z_{X} values are approximately distributed as a Gaussian, with the exception of two high redshift values (see Figure 3). However, due to the estimated uncertainties, the probability of a uniform redshift distribution across the ICM is still high at the 24% level ($\chi^2 = 12.70$ for 10 dof), which implies no significant detection (less than 2σ) of global bulk motions. Formally, we measure an average bulk motion of $v_{\text{BM}} = 1700 \pm 840$ km/s. In addition, the projected redshift map shows that the two high redshift regions 4 and 9 are contiguous (see Figure 4, lower panels), and this can be interpreted with an enhanced likelihood of a redshift difference between the diffuse emission in the north and the main halo. The average redshift of regions 4 and 9 is 0.1310, while that of the other regions is 0.1081. This implies a velocity difference of $\Delta v_{\text{max}} = 6200 \pm 3300$ km/s. The presence of two distinct halos with different redshift may suggest a classification as a pre-merger. Due to the presence of a well developed shock, this cluster may be caught in the early stages of the merger process, in line with the conclusion of Owers et al. (2014) who estimate that the merger is observed only ~ 0.3 Gyr after core-passage.

4.3. Abell 115

Abell 115 has been classified a merger on the basis of its double X-ray morphology (Forman et al. 1981). The ICM thermal structure is best described by two halos which host a cool core, with a significantly hotter gas between and around them, suggesting that the system is in an advanced stage of merging, despite no shock front has been found in this region (Shibata et al. 1999; Gutierrez & Krawczynski 2005). A dynamical analysis based on 88 cluster member spectra (Barrena et al. 2007) shows a line-of-sight velocity difference of 1646 km/s between the northern and southern subclusters at a projected separation of 0.89 Mpc. In addition, Barrena et al. (2007) interpret the system as being a pre-merger based on the location of the BCG's consistent with the peaks in the X-ray surface brightness distribution. Diffuse radio emission north of the cluster has been found by Govoni et al. (2001) with a 1.4 GHz VLA observation and interpreted as a radio relic possibly associated to the ongoing merger. Abell 115 is also included in the Merging Cluster Collaboration sample.

We used 4 ACIS-I observations contiguous in time, for a total of 310.6 ks. The total number of counts in the 0.5-10 keV band within a circle of 5.2 arcmin in the merged image is 2.88×10^5 . This allows us to obtain 18 regions useful for spectral analysis. Our spatially resolved spectroscopic analysis provides us with reliable z_{X} only in 12 regions out of 18. The average redshift $\langle z_{\text{X}} \rangle = 0.1979$ is in good agreement with $z_{\text{opt}} = 0.197$ (Hiroi et al. 2013) while the global redshift $z_{\text{Xtot}} = 0.1892^{+0.003}_{-0.004}$ is significantly lower. To evaluate systematic uncertainties on z_{X} we consider a temperature and abundance range of 2-12 keV and 0.2-0.9 Z_{\odot} , respectively. The best-fit z_{X} of the 12 regions used in our analysis with corresponding errors are listed in Table 7.

The hypothesis of a constant redshift across the 12 regions is rejected at more than 3σ ($\chi^2 = 30.4$ for 11 dof). The histogram distribution of z_{X} (see Figure 5) shows the presence of two regions significantly above and below the central value. We measure an average bulk motion velocity of $v_{\text{BM}} = 4600 \pm 1100$ km/s.

A visual inspection of the redshift map and significance map (see Figure 6, lower panels) allows us to identify three main regions with compatible redshift. We first isolate regions belonging to the northern clump (regions 0, 1, 2, 4 and 10) and to the southern clump (3, 6, 11, 17, and 15). We find a redshift difference which corresponds to about 1σ , therefore consistent with having the same redshift. Formally, translated into a velocity difference, this would imply a relative velocity of 3300 ± 3200 km/s. If we consider instead regions 12 and 14, we find an average redshift of 0.1634, corresponding to a velocity difference of 8600 ± 3000 km/s with respect to the bulk of the ICM. We remark that this is also the gas which is found to be significantly hotter (at least by a factor of two, as verified in the projected temperature map not discussed here), and therefore it is likely to be heated and violently displaced by the ongoing merger. This is consistent with a substantial amount of the shocked gas being compressed between the two halos and pushed towards the observer, with the two halos having a minimum in the velocity difference. Therefore, we conclude that A115 is caught in the early phase of the merging process, with the two ICM halos still well separated.

4.4. Abell 520

Abell 520, at $z_{\text{opt}} = 0.203$ (Cassano et al. 2013), was found to host a radio halo elongated in the NE-SW direction, corresponding to the apparent merger axis (Giovannini et al. 1999;

⁵ <http://www.mergingclustercollaboration.org/>

Govoni et al. 2001). The X-ray morphology and the optical spectroscopy suggest a disturbed dynamical state (Govoni et al. 2001; Proust et al. 2000, respectively). Despite the recent in-depth studies (Mahdavi et al. 2007; Girardi et al. 2008) the detailed structure of the merger of Abell 520 is still unclear. However, a prominent bow shock with $M = 2.1^{+0.4}_{-0.3}$ has been identified thanks to *Chandra* data analysis (Markevitch et al. 2005b). Abell 115 is also included in the Merging Cluster Collaboration sample.

A520 has the longest *Chandra* ACIS-I exposure for a total of 516.4 ks. The number of net counts in the 0.5-10 keV band in the merged image is 3.36×10^5 in a circle of 3.2 arcmin radius. The best-fit redshift from the global emission is $z_{\text{Xtot}} = 0.2082^{+0.0046}_{-0.0049}$. To estimate the systematic uncertainty on z_{X} we consider a range of 3-15 keV and 0.2-1 Z_{\odot} for temperature and abundance, respectively.

We discard only two regions which do not provide a reliable redshift. Therefore we base our analysis on 18 regions, whose best-fit z_{X} and associated errors are listed in Table 8. The average redshift among those regions is $\langle z_{\text{X}} \rangle = 0.2083$ in good agreement with z_{Xtot} and z_{opt} . The hypothesis of a constant redshift is rejected at $\sim 87\%$ confidence level ($\chi^2 = 23.4$ for 17 dof), therefore less than 2σ . We find $v_{\text{BM}} \sim 1800 \pm 900$ km/s. This is mostly contributed by the presence of blueshifted regions, mostly in the central 1 arcmin, and the surrounding higher redshift regions, as is possible to see comparing the histogram distribution (see Figure 7) with the redshift and significance maps (see Figure 8). If we compute the difference between the two sets of regions with comparable redshift, we find $\Delta v_{\text{max}} = 5900 \pm 4000$ km/s. The overall redshift map suggests a merger with an halo moving towards the observer, caught shortly after the first pericentric passage.

4.5. 1RXS J0603.3+4214

1RXS J0603.3+4214 (the “Toothbrush” cluster) at redshift $z_{\text{opt}} = 0.225$ (van Weeren et al. 2012) was discovered in the radio band thanks to its prominent linear radio relic and radio halo plus several additional features which suggest this is a complex merger. Simulations also show that the merger might be a triple process: in addition to the northern and southern subclusters with similar mass, there might be another smaller subcluster infalling in the south (Brüggen et al. 2012). Measurement of the radio spectral index allowed van Weeren et al. (2012) to constrain the merger Mach number in the range 3.3-4.6. However, X-ray observation by *XMM-Newton* returned a Mach number < 2 (Ogorean et al. 2013) inconsistent with the radio constraints. 1RXS J0603.3+4214 is also included in the Merging Cluster Collaboration sample.

We use three *Chandra* ACIS-I observations for a total of 235.9 ks. The total number of counts in the 0.5-10 keV band within a circle of 3.5 arcmin is 1.74×10^5 in the merged image. To evaluate the systematic uncertainty on z_{X} we consider a range of 8-16 keV and 0.3-0.8 Z_{\odot} for temperature and abundance, respectively. We are able to obtain reliable spectral fit in 8 out of 9 regions originally considered for analysis. The best-fit z_{X} and corresponding errors are listed in Table 9. The average redshift across the regions is $\langle z \rangle = 0.2303$, in good agreement with $z_{\text{Xtot}} = 0.2316^{+0.0029}_{-0.0033}$ and in reasonable agreement with z_{opt} . The hypothesis of a constant redshift is acceptable, as shown also by the histogram distribution of best-fit z_{X} values shown in Figure 9 ($\chi^2 = 8.7$ for 7 dof). The upper limit to the average bulk motion velocity is $v_{\text{BM}} < 2100$ km/s. However there is a significant uniform gradient in the best-

fit redshift from the northern (high- z) to the southern (low- z) clump (see Figure 10), which corresponds to a maximum difference of $\sim 0.0295 \pm 0.0115$, or a maximum velocity difference of $\Delta v_{\text{max}} \sim 7200 \pm 2800$ km/s. On the basis of these results, this cluster can be classified as a pre-merger.

4.6. Abell 2146

Despite the lack of diffuse radio emission, A2146 is classified as an extreme binary, head-on cluster merger in Mann & Ebeling (2012). A deep *Chandra* study revealed the presence of two shock fronts with Mach numbers $M = 2.2 \pm 0.8$ and $M \sim 1.7 \pm 0.3$ (Russell et al. 2010). Using the radial velocity of BCGs in the subcluster and the main cluster, Canning et al. (2012) find that the merger axis has an angle of 17° with respect to the plane of the sky. For these properties and its appearance in the X-ray, Abell 2146 is often compared to the Bullet cluster.

We use the observations with *Chandra* ACIS-I for a total of 375.3 ks, as listed in Table 1. For simplicity we do not consider observations with ACIS-S for a total of 45 ks, in order to keep a uniform calibration throughout our analysis, given the smaller amount of observing time contributed by the ACIS-S exposures. The total number of net counts in the 0.5-10 keV band within a circle of 3.6 arcmin is about 1.99×10^5 . The best fit redshift obtained fitting the total X-ray emission is $z_{\text{Xtot}} = 0.2310^{+0.0022}_{-0.0010}$. Measured temperatures range from the inner ~ 3 keV to the outer ~ 8 keV in our analysis of the temperature structure (not reported in this work). To evaluate the systematic uncertainty on z_{X} we consider ranges from 1 to 12 keV and 0.15 to 1.5 Z/Z_{\odot} to explore the temperature and metal abundance throughout the ICM, respectively.

We are able to obtain a reliable spectral fit in 17 out of 19 regions originally selected in the X-ray image. The best-fit z_{X} of the regions used in our analysis with the corresponding statistical and systematic errors are listed in Table 10. The average redshift across the region is $\langle z_{\text{X}} \rangle = 0.2338$, which is consistent with z_{Xtot} within 1σ . We find a $\chi^2 = 19.68$ for 16 degrees of freedom, as listed in Table 4, pretty much consistent with a constant redshift across the ICM. The histogram distribution of z_{X} , shown in Figure 11, is consistent with a Gaussian dominated by noise and shows no clear evidence of bulk motions. The average bulk motion is formally $v_{\text{BM}} = 480 \pm 490$ km/s. The projected X-ray redshift map and significance map are shown in Figure 12. The maximum redshift difference is $\Delta v_{\text{max}} = 8200 \pm 3600$ km/s, and it is obtained between two distinct regions with homogeneous redshift: the “bullet” and its trail, along the direction of the merger, which are blueshifted with respect to the average redshift, and all the surrounding ICM emission, which is redshifted. Despite the low S/N, the redshift map is depicting a clear dynamical situation where the central ICM is dominated by an halo moving towards the observer while the larger scale emission has, in average, a larger redshift. This provides support to the presence of bulk motions, still dominated by the infall velocity of the merging halos.

4.7. Abell 1689

Abell 1689 is a typical relaxed cluster at $z \sim 0.183$ (Hiroi et al. 2013). We reduced and analyzed four ACIS-I observations for a total of 151.3 ks (see Table 2). The total number of net counts in the 0.5-10 keV band within a circle of 1 arcmin is about 1.86×10^5 in the ACIS-I merged image. The best fit redshift obtained fitting the total X-ray emission is

$z_{\text{Xtot}} = 0.1814^{+0.0028}_{-0.0008}$. To evaluate the systematic uncertainty on z_X we consider ranges from 5 to 15 keV and 0.3 to 0.9 Z/Z_\odot to explore the temperature and metal abundance throughout the ICM, respectively.

We are able to obtain a reliable spectral fit in all the 10 regions originally selected in the X-ray image. The best-fit z_X of the regions used in our analysis with the corresponding statistical and systematic errors are listed in Table 11. The average redshift across the region is $\langle z_X \rangle = 0.1814$. The histogram distribution of z_X , shown in Figure 13, is consistent with a Gaussian distribution whose σ is the average statistical error on z_X . We find $\chi^2 = 9.31$ for 9 degrees of freedom, as listed in Table 4. Therefore we do not find any hint of bulk motion, as expected, and find a hard upper limit of $v_{\text{BM}} < 1600$ km/s.

4.8. Abell 1835

Abell 1835 is a relaxed cluster at $z \sim 0.234$ (Girardi et al. 2014). We reduced and analyzed three ACIS-I observations for a total of 193.7 ks (see Table 2). The total number of net counts in the 0.5–10 keV band within a circle of 1 arcmin is about 2.33×10^5 in the ACIS-I merged data. The best fit redshift obtained fitting the total X-ray emission is $z_{\text{Xtot}} = 0.2478^{+0.0021}_{-0.0012}$, significantly larger than the optical value. To evaluate the systematic uncertainty on z_X we consider ranges from 4 to 14 keV and 0.2 to 0.8 Z/Z_\odot to explore the temperature and metal abundance throughout the ICM, respectively.

We are able to obtain a reliable spectral fit in all the 11 regions originally selected in the X-ray image. The best-fit z_X of the regions used in our analysis with the corresponding statistical and systematic errors are listed in Table 12. The average redshift across the region is $\langle z_X \rangle = 0.2483$. The histogram distribution of z_X , shown in Figure 15, is consistent with a Gaussian distribution whose σ is the average statistical error on z_X . We find $\chi^2 = 11.5$ for 10 degrees of freedom, as listed in Table 4. Therefore we do not find any hint of bulk motion, as expected, and find a hard upper limit of $v_{\text{BM}} < 1350$ km/s.

5. STATISTICAL PROPERTIES OF THE CLUSTER SAMPLE

In Figure 17 we summarize our results, showing the χ^2 values vs the degrees of freedom for all the clusters analysed in this work and listed in Table 4. The comparison with the lines corresponding to 1, 2 and 3 σ confidence levels, shows that, in general, merging clusters always have a larger probability of showing bulk motions in their ICM, but only in two cases we have a statistical significance larger than 3 σ . In two cases, instead, the probability is less than 2 σ , and, finally, in the last two cases the global χ^2 is not significantly different from that of the two relaxed clusters, which show no signs of bulk motions. Globally, the merging cluster sample always shows a larger probability of hosting bulk motions, but it is hard to reach definitive conclusions in single cases.

However, we remark that the analysis simply based on the χ^2 including all the ICM regions tends to dilute the signal, since the majority of the ICM regions are expected to show no significant bulk motions, considering that only few, large mass of ICM displaced at large velocity during the merger process can give origin to the bulk motion signal, not to mention projection effects which may erase the signal. On the bright side, our global evaluation of bulk motion is free from the “look-elsewhere effect” (Lyons 2008). We conclude that, under our most conservative assumptions, only a fraction of the major mergers shows unambiguous signatures of bulk motions in *Chandra* CCD data. Specifically, we measure

$v_{\text{BM}} = 1400 \pm 300$ and 4600 ± 1100 km/s in A2142 and A115, respectively. In A2034 and A520 we find $v_{\text{BM}} = 1700 \pm 840$ and 1800 ± 900 , respectively, despite this measurement is not significant (less than 2 σ). In the case of 1RXSJ0603.3+4214 and A2146 we find a hard (corresponding to 3 σ) upper limit of 2100 and ~ 1500 km/s, respectively. These limits are similar to those found for the two relaxed clusters A1689 and A1835, where we find $v_{\text{BM}} < 1600$ and $v_{\text{BM}} < 1350$ km/s, respectively.

Local velocity differences between ICM regions may achieve much larger values, with corresponding larger errors. In the 8th columns of Table 4 we list the values of Δv_{max} found by identifying the ICM regions (or groups of regions) with the largest difference in z_X . Clearly, this does not constitute a detection of bulk motion, however, it gives a rough estimate of the maximum velocity difference we can have across the ICM in our data.

The visual inspection of the redshift and significance maps allows us also to provide a rough classification in terms of pre-merger or ongoing/post-merger. The first case is when two comparable-mass halos are about to start head-on merger with large speed along the line of sight, so that in the redshift map the two halos appear to have clearly distinct average redshift (see, for example, the case of 1RXSJ0603.3+4214). The ongoing or post-merger case is when shocks in the ICM are clearly present, and the first pericentric passage is recent (i.e., it happened since less than one dynamical time, see A2034 and A115). Given the uncertainties on the bulk motion velocity, we are not able to explore the regime when the residual kinetic energy of the merger event already decreased to a more diffuse and chaotic turbulent velocity field of the order of few $\times 100$ km/s. Our qualitative classification is also provided in the last columns of Table 4.

6. DISCUSSION AND FUTURE PROSPECTS

In this work we use the same conservative approach we adopted also in Liu et al. (2015), where we explored the presence of bulk motions in the ICM of 1E0657-56. In particular, when estimating the statistical significance of bulk motions, we used five conservative assumptions:

- we considered only the Fe line emission in the hard band, while the use of the soft band would have significantly reduced the statistical error on z_X , particularly for the cold regions. However, since, in principle, gas with different temperatures can have different position along the line of sight and different velocity, this may introduce a source of scatter in z_X which is hard to control;
- we computed the total error on z_X in each region summing in quadrature the statistical error and the 90% percentile of the z_X distribution obtained by imposing a varying thermal structure in the ICM. This systematic component is often smaller or at best comparable to the statistical component. The systematic component is likely to be slightly overestimated, as we can verify by comparing σ_{rms} of the z_X distribution with the average total error $\langle \sigma_{\text{tot}} \rangle$;
- we discarded all the regions where the best-fit redshift is not identified clearly, rejecting all the spectra where the C_{stat} vs redshift plot shows a secondary minimum at a distance $\Delta C_{\text{stat}} < 6.6$ from the absolute minimum;

TABLE 4

THE RESULTS OF THE χ^2 TEST ON THE DISTRIBUTION OF REDSHIFT OF THE CLUSTERS, AND CORRESPONDING CONSTRAINTS ON v_{BM} AND Δv_{max} IN KM/S. THIS INFORMATION IS COMBINED WITH VISUAL INSPECTION OF THE REDSHIFT MAPS TO OBTAIN THE QUALITATIVE CLASSIFICATION LISTED IN THE LAST COLUMN.

| Cluster name | z_{Xtot} | $\langle z_{\text{X}} \rangle$ | degrees of freedom ($N_{\text{reg}}-1$) | χ^2 | prob of BM | v_{BM} km/s | Δv_{max} km/s | classification |
|---------------|------------------------------|--------------------------------|--|----------|------------|-------------------------|---------------------------------|--------------------|
| A2142 | $0.0852^{+0.0012}_{-0.0009}$ | 0.0855 | 46 | 88.02 | 99.98% | 1400 ± 300 | 7400 ± 2200 | post-merger |
| A2034 | $0.1124^{+0.0039}_{-0.0044}$ | 0.1122 | 10 | 12.70 | 76% | 1700 ± 840 | 6200 ± 3300 | pre/ongoing merger |
| A115 | $0.1892^{+0.0030}_{-0.0040}$ | 0.1979 | 11 | 30.4 | 99.9% | 4600 ± 1100 | 8600 ± 3000 | pre/ongoing merger |
| A520 | $0.2082^{+0.0046}_{-0.0049}$ | 0.2083 | 17 | 23.4 | 86% | 1800 ± 900 | 5900 ± 4000 | post-merger |
| 1RXSJ060313.4 | $0.2316^{+0.0029}_{-0.0033}$ | 0.2303 | 7 | 8.6 | 72% | < 2100 | 7200 ± 2800 | pre-merger |
| A2146 | $0.2310^{+0.0022}_{-0.0010}$ | 0.2338 | 16 | 19.68 | 77% | 480 ± 490 | 8200 ± 3600 | pre/ongoing merger |
| A1689 | $0.1814^{+0.0028}_{-0.0008}$ | 0.1814 | 9 | 9.3 | 59% | < 1600 | 4600 ± 3000 | relaxed |
| A1835 | $0.2478^{+0.0021}_{-0.0012}$ | 0.2483 | 10 | 11.5 | 38% | < 1350 | 4200 ± 2600 | relaxed |

- despite the signature of bulk motion is presumably confined to few, largely discrepant regions, we evaluate the statistical significance with a simple χ^2 test on all the regions. This of course would dilute the effect, but provides a robust evaluation of the actual presence of bulk motions completely free from the “look-elsewhere effect” (Lyons 2008);
- we use information from the spatial distribution of z_{X} only to provide a qualitative description of the possible dynamical status of the cluster, and not to reinforce the statistical significance of the z_{X} fluctuations. In practice, we do not re-define regions to merge them together according to their z_{X} value, a procedure that would reduce the statistical uncertainty on the final z_{X} maps.

Given our extremely conservative approach, we only hit the tip of the iceberg of the signatures of bulk motions in *Chandra* CCD data. Our results show, at the same time, the difficulty in measuring bulk motions, but also the widespread presence of bulk motions in massive, head-on mergers.

Based on this tantalizing but promising results, in the next future we plan to relax some of these constraints. In particular, we will include the soft band spectral information, and investigate quantitatively the spatial correlation of z_{X} fluctuations, possibly merging projected ICM region which have similar redshift, on the basis of the spectral analysis and surface brightness features. In addition, we can also combine X-ray spectrally resolved analysis with dynamical studies based on the optical redshift distribution of the member galaxies. We are currently applying the caustic method (Diaferio 1999; Diaferio et al. 2005; Serra & Diaferio 2013; Yu et al. 2015) to a few nearby, massive clusters in the Abell cluster catalog (Abell et al. 1989), with the aim of carefully comparing the optical dynamical structure to the X-ray morphology and spatially resolved spectral analysis (Yu et al., in preparation).

Clearly, any improvement which can be possibly achieved with current facilities is limited by the modest spectral resolution. In particular, the inevitable superposition of ICM massive regions with different redshift along the line of sight heavily blurs the redshift map. Sometimes, the presence of more than one minima in CCD spectra may be interpreted, in principle, as the superposition of two ICM regions moving at different redshift. However, it is impossible to reach this kind of conclusion with the current coarse spectral resolution. In the next future, the X-ray bolometer on board of Astro-H (Takahashi et al. 2014) will provide ICM spectra with very high resolution along the line of sight, so that the velocity regime probed in the ICM will reach few $\times 100$ km/s as op-

posed to the current limit of ~ 2000 km/s. However, the lack of adequate spatial resolution will still make the *Chandra* data a crucial complementary source of information to explore the ICM dynamics in the next years.

7. CONCLUSIONS

We search for bulk motions in the ICM in a sample of 6 clusters at $0.1 < z < 0.3$ classified as massive mergers on the basis of their X-ray morphology, diffuse radio emission or dynamical optical substructure, plus 2 relaxed clusters. By performing spatially resolved spectral analysis on *Chandra* CCD data, we obtain the distribution of ICM redshift z_{X} across their ICM, after a careful and extremely conservative evaluation of the total error on each z_{X} value. We accurately investigate the distribution of z_{X} , the z_{X} map and finally obtain a robust estimate of bulk motions in the ICM. Considering the global distribution of z_{X} across the ICM, our analysis shows that for 2 of the 6 merger clusters we find significant evidence of bulk motions at more than 3σ at the level of $v_{\text{BM}} = 1400 \pm 300$ and 4600 ± 1100 km/s in A2142 and A115, respectively. We also obtain a measurement at lower significance (less than 2σ) of $v_{\text{BM}} = 1700 \pm 840$ and 1800 ± 900 in A2034 and A520, respectively. Finally for 2 clusters (1RXSJ0603.3+4214 and A2146) the global analysis of the z_{X} distribution is not significantly different from that of 2 relaxed clusters (A1689 and A1835), where we do not find any signs of bulk motion, as expected.

Eventually, we consider specific regions by combining the z_{X} distribution with the redshift maps, and we are able to identify regions which show relevant bulk motion velocities in all the merger clusters. We identify local velocity differences between ICM regions ranging from 5900 to 8600 km/s, with a typical uncertainty of 30-50%. Whenever possible we use the spatial distribution of z_{X} to infer a qualitative description of the dynamical status of the clusters, tentatively classifying them as pre-merger, ongoing or post-merger. Our results are summarized in Table 4.

We conclude that *Chandra* data can be successfully used to detect ICM bulk motions in massive merging clusters at $0.1 < z < 0.3$. Unfortunately, the CCD coarse spectral resolution make it impossible to provide a meaningful reconstruction of the velocity field of the ICM in single clusters. However, as soon as high-resolution, spatially resolved X-ray spectroscopy will be available, the ICM dynamics will become a key diagnostics to understand the dynamics of the whole clusters, the physics of the ICM itself, to achieve accurate measurement of the total mass, and, ultimately, to perform accurate cosmological test based on cluster abundance. We are currently planning a refined strategy to carefully relax

some of our assumptions, and possibly reach a lower velocity regime with current CCD data. The hard-limit imposed by the spectral resolution can be partially overcome by next-future X-ray bolometers. However, due to the low angular resolution of X-ray bolometers, *Chandra* data will be a key complementary probe for ICM dynamics in the next years.

This work was supported by the Chinese Ministry of Science and Technology National Basic Science Program (Project 973) under Grant No.2012CB821804 and 2014CB845806, the Strategic Priority Research Program “The Emergence of Cosmological Structure” of the Chinese Academy of Sciences (No. XDB09000000), the National Natural Science Foundation of China under Grants Nos. 11373014, 11073005, and 11403002, the Fundamental Research Funds for the Central Universities and Scientific Research Foundation of Beijing Normal University. P.T. is supported by the Recruitment Program of High-end Foreign Experts and he gratefully acknowledges hospitality of Beijing Normal University. A.L. is supported by the NSF grant AST-1413056.

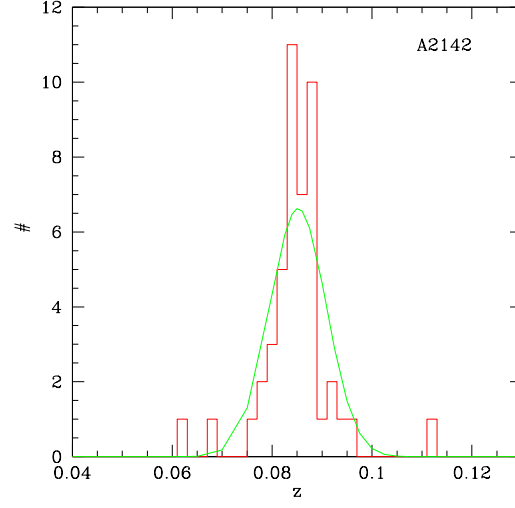


FIG. 1.— Histogram distribution (solid red line) of the best-fit z_X for the 47 regions of Abell 2142 with reliable spectral fit. The green line is the Gaussian with $\sigma_G = \langle \sigma_{\text{tot}} \rangle$ centered on $\langle z_X \rangle$.

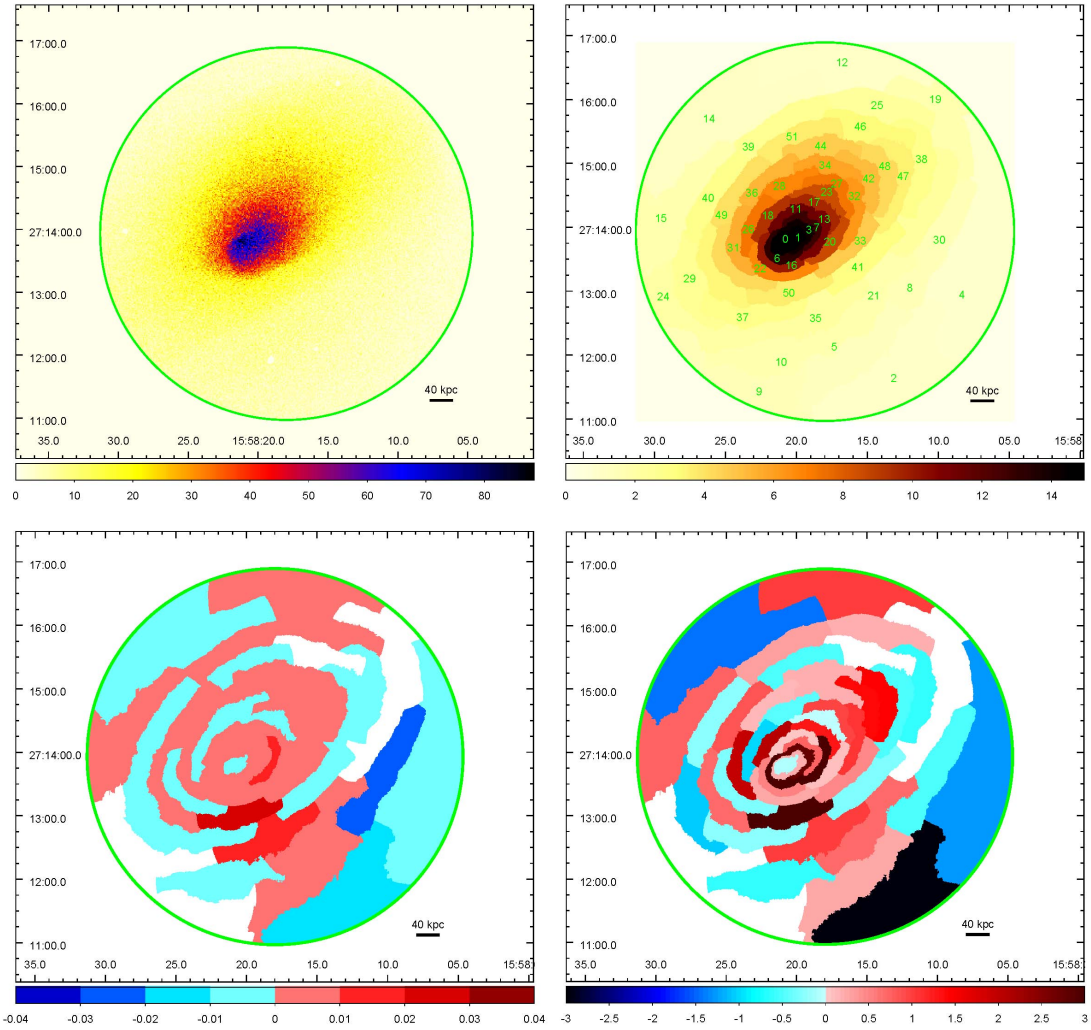


FIG. 2.— Top left panel: Surface brightness distribution of Abell 2142 in the 0.5-10 keV band; top right panel: region map; bottom left panel: redshift map; bottom right panel: significance map. White regions do not have a reliable redshift measurement.

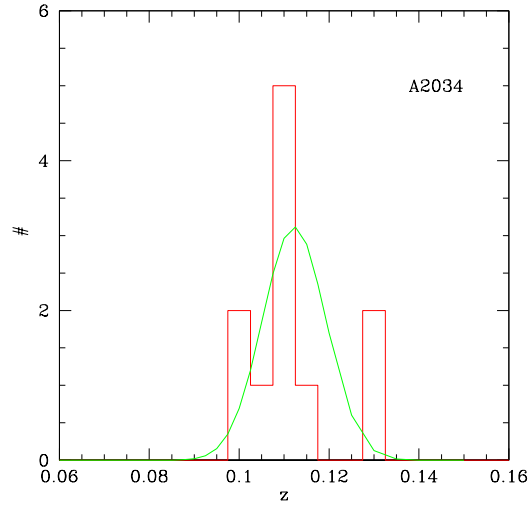


FIG. 3.— Histogram distribution of the best-fit z_{χ} for the 11 regions of Abell 2034 with reliable spectral fit. Lines as in Figure 1.

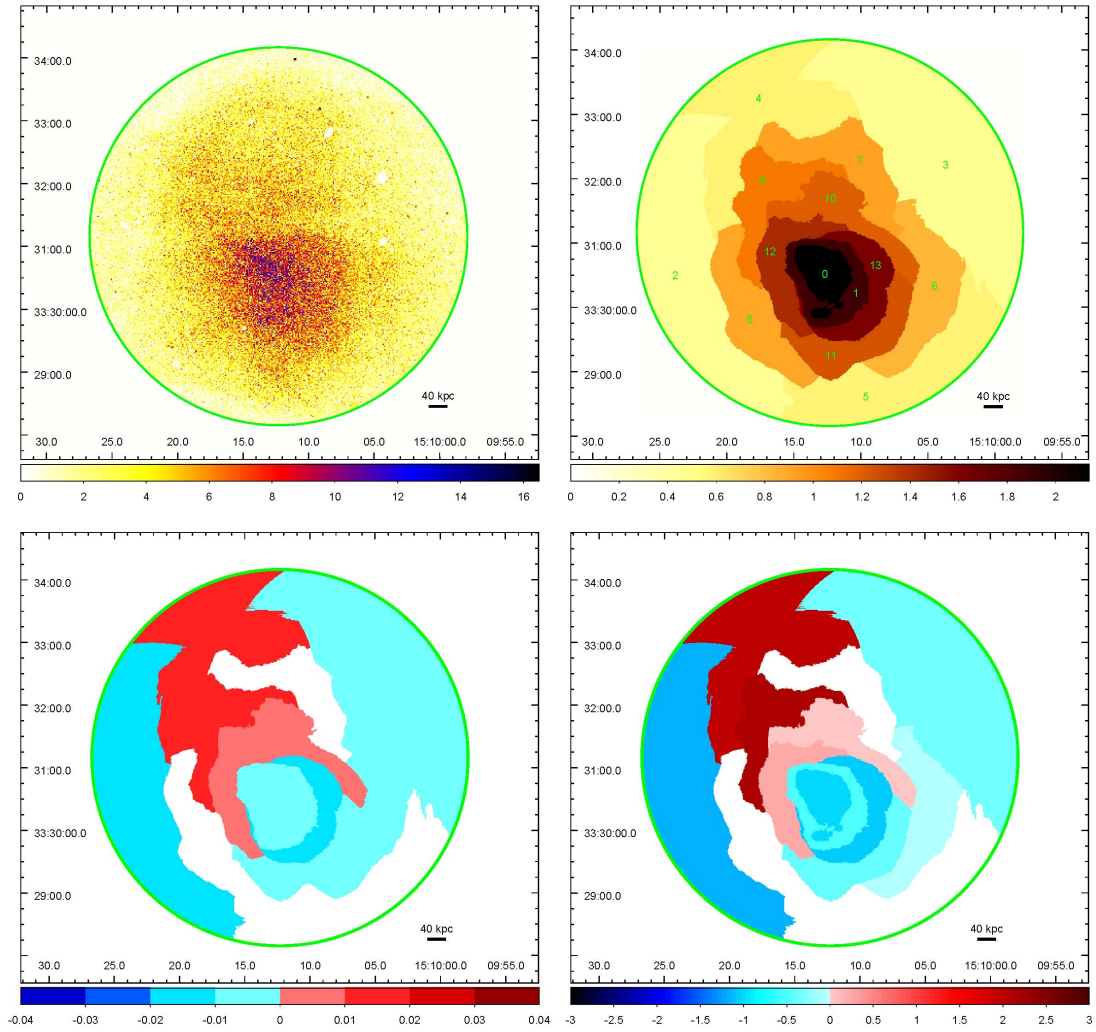


FIG. 4.— Same as Figure 2 for Abell 2034.

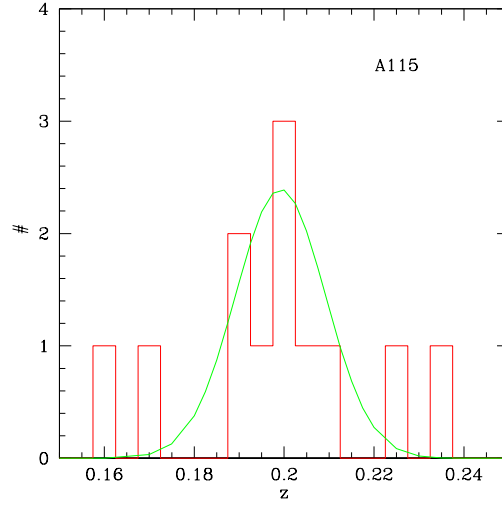


FIG. 5.— Histogram distribution of the best-fit z_{χ} for the 12 regions of Abell 115 with reliable spectral fit. Lines as in Figure 1.

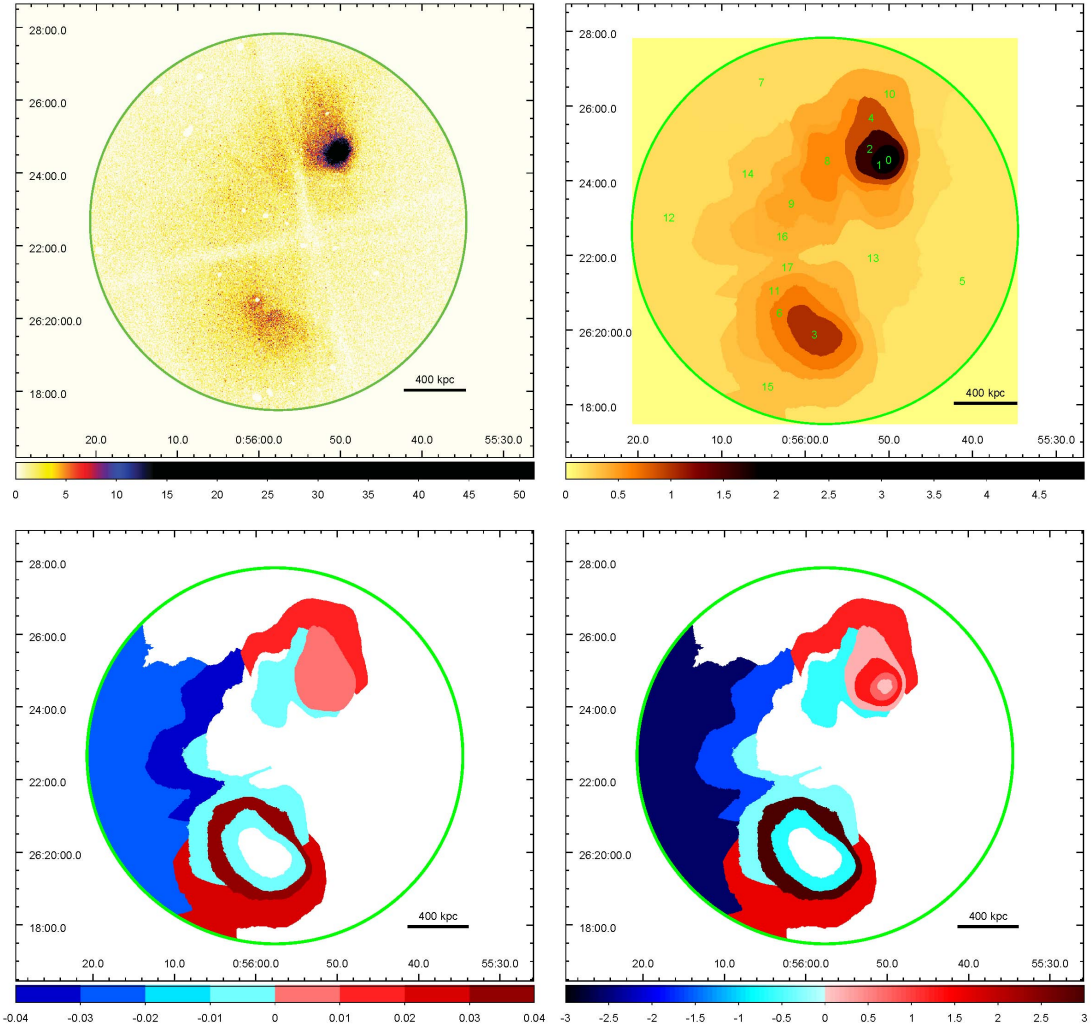


FIG. 6.— Same as Figure 2 for Abell 115.

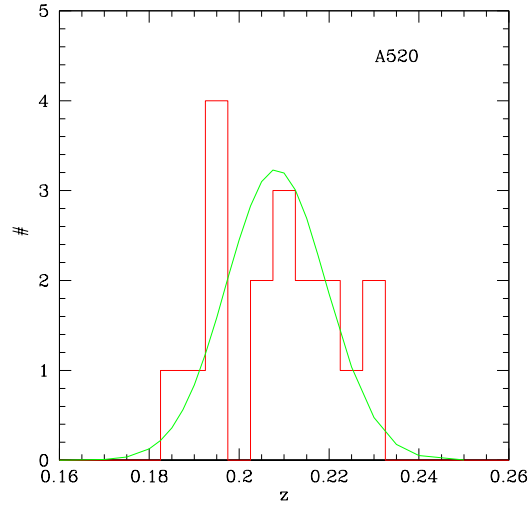


FIG. 7.— Histogram distribution of the best-fit z_{χ} for the 18 regions of Abell 520 with reliable spectral fit. Lines as in Figure 1.

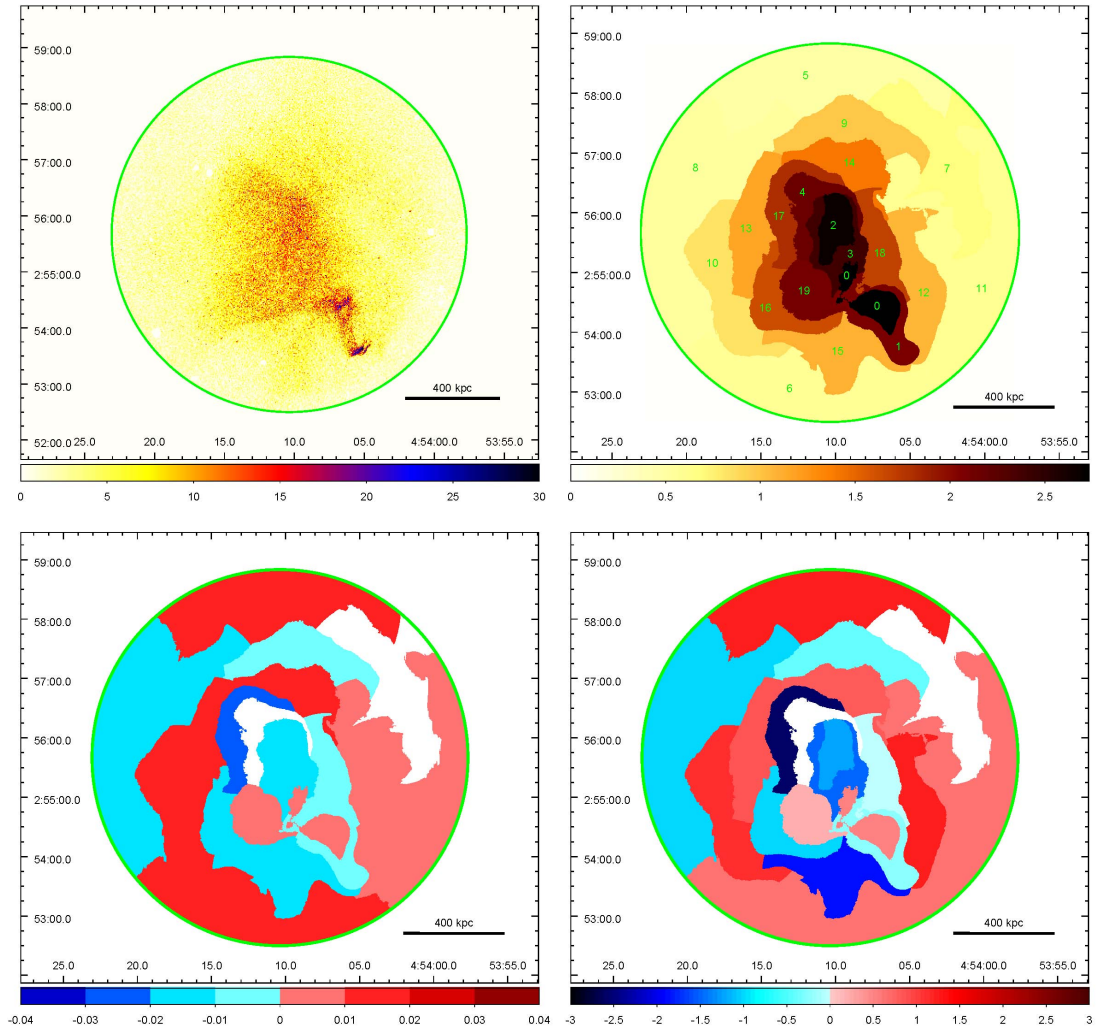


FIG. 8.— Same as Figure 2 for Abell 520.

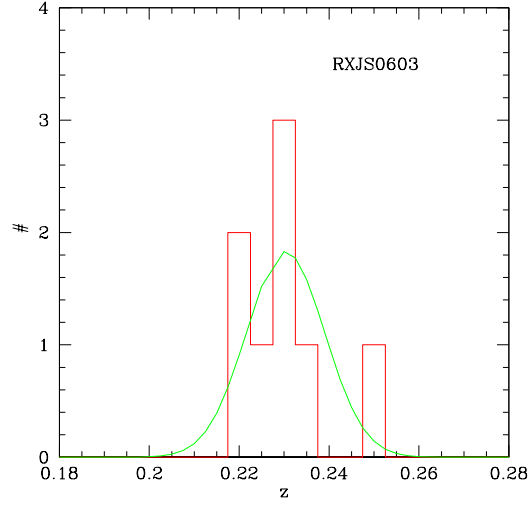


FIG. 9.— Histogram distribution of the best-fit z_{χ} for the 8 regions of 1RXSJ0603.3+4214 with reliable spectral fit. Lines as in Figure 1.

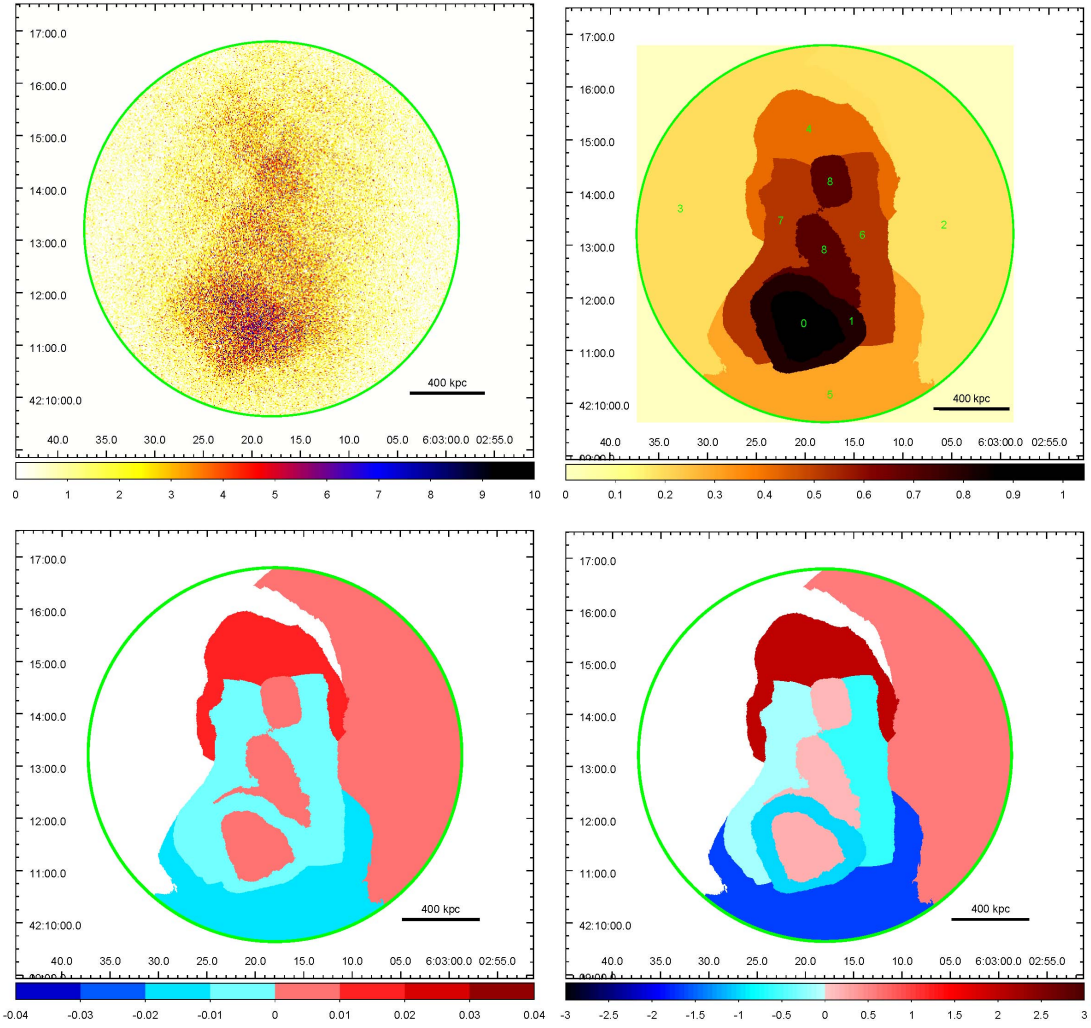


FIG. 10.— Same as Figure 2 for 1RXSJ0603.3+4214.

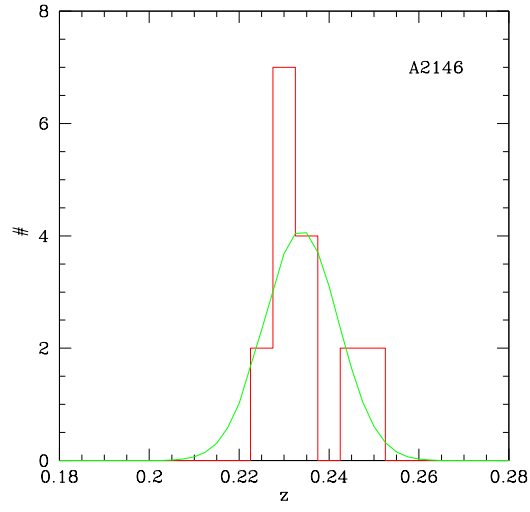


FIG. 11.— Histogram distribution of the best-fit z_X for the 17 regions of A2146 with reliable spectral fit. Lines as in Figure 1.

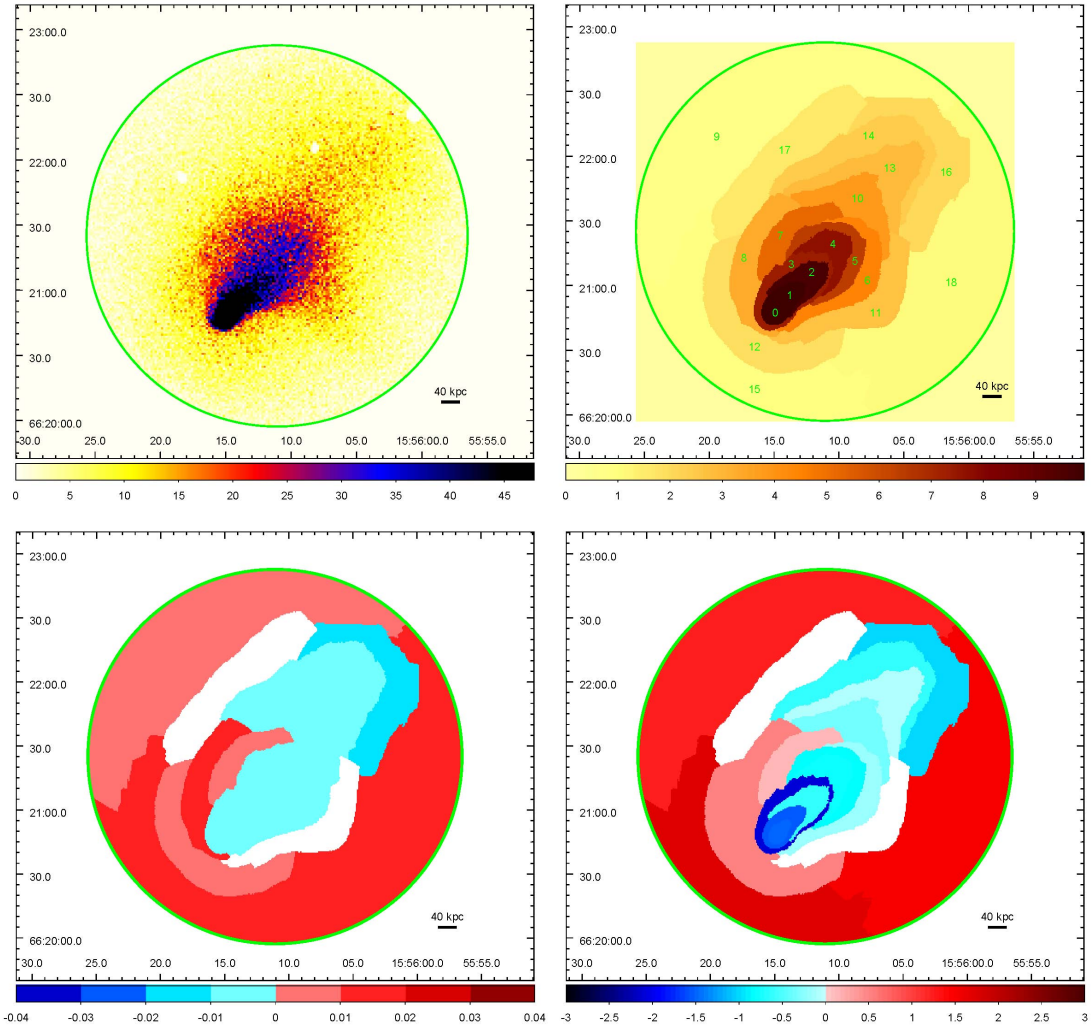


FIG. 12.— Same as Figure 2 for Abell 2146.

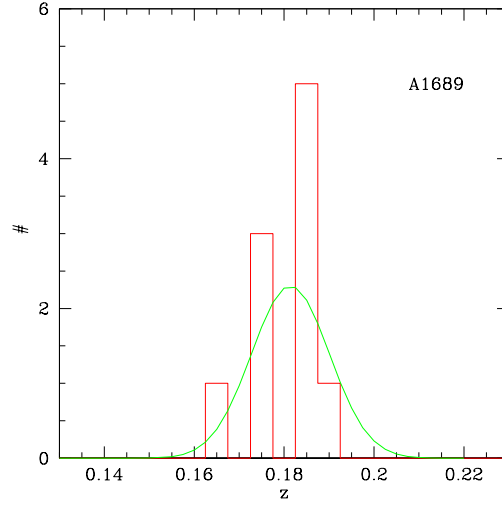


FIG. 13.— Histogram distribution of the best-fit z_X for the 10 regions of A1689 with reliable spectral fit. Lines as in Figure 1.

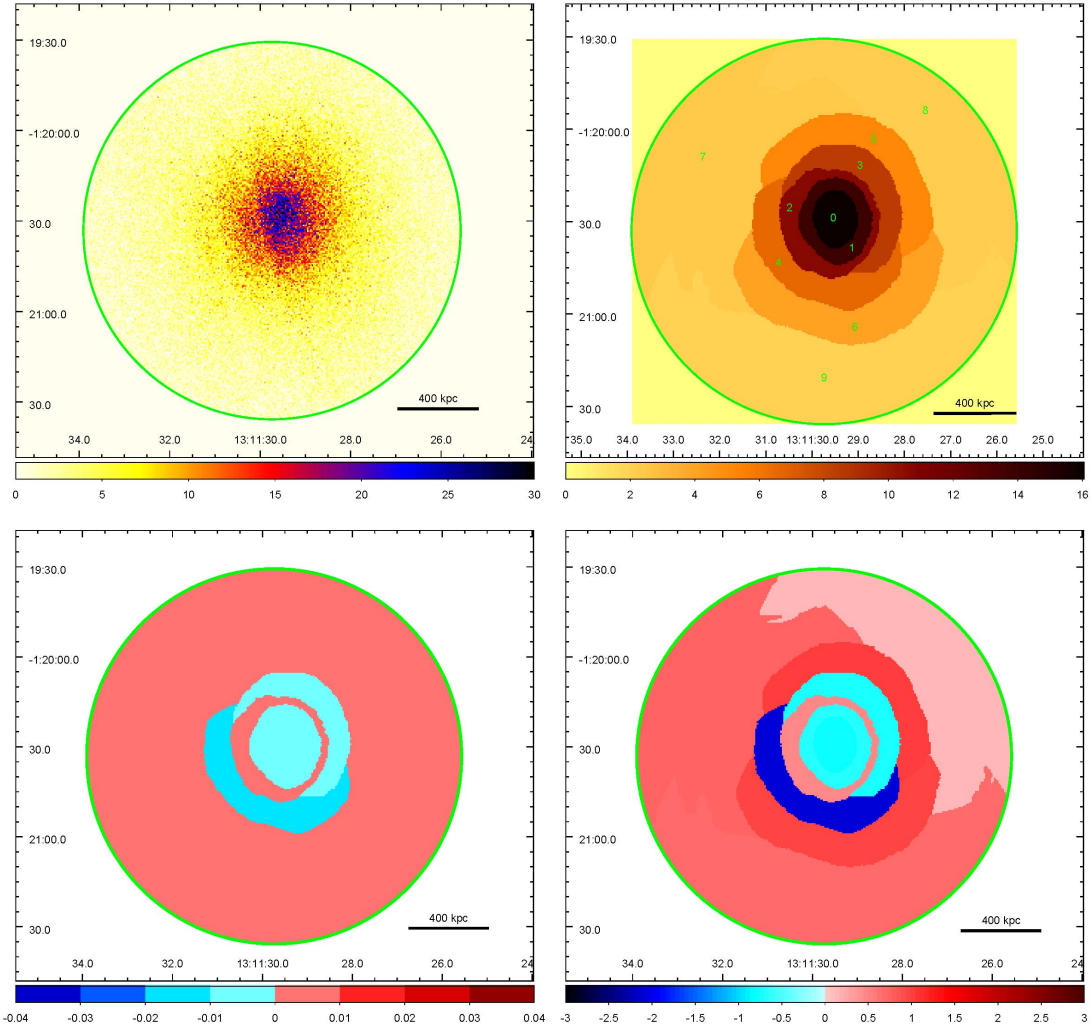


FIG. 14.— Same as Figure 2 for Abell 1689.

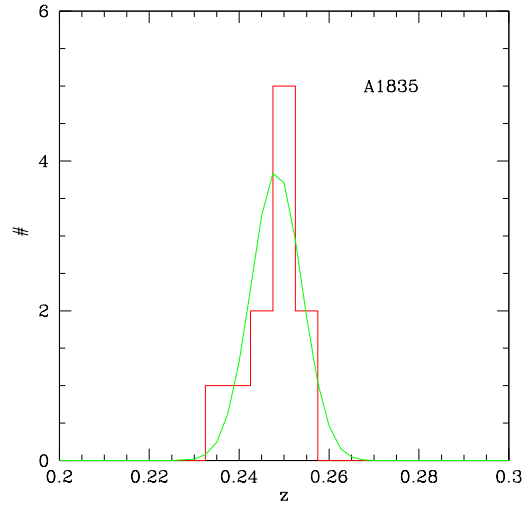


FIG. 15.— Histogram distribution of the best-fit z_X for the 11 regions of A1835 with reliable spectral fit. Lines as in Figure 1.

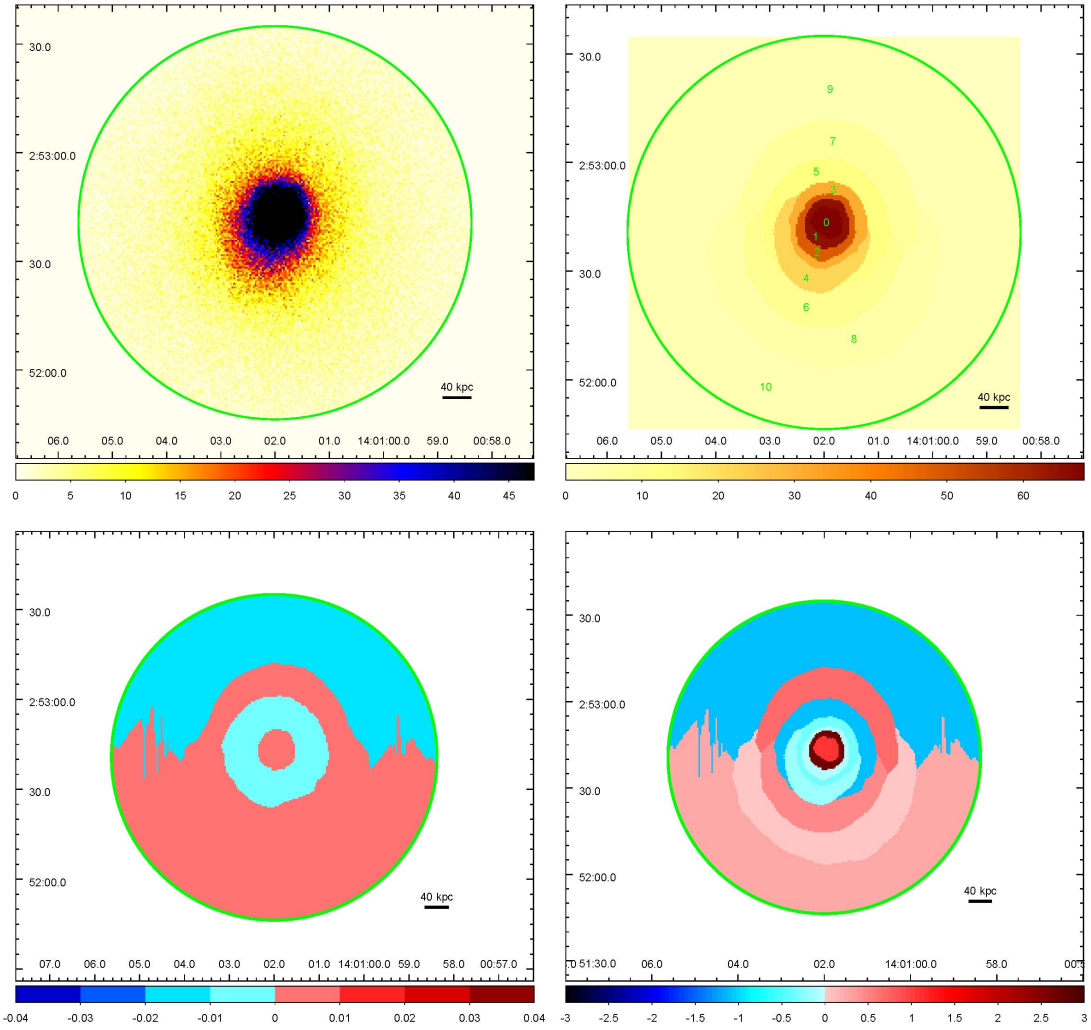


FIG. 16.— Same as Figure 2 for Abell 1835.

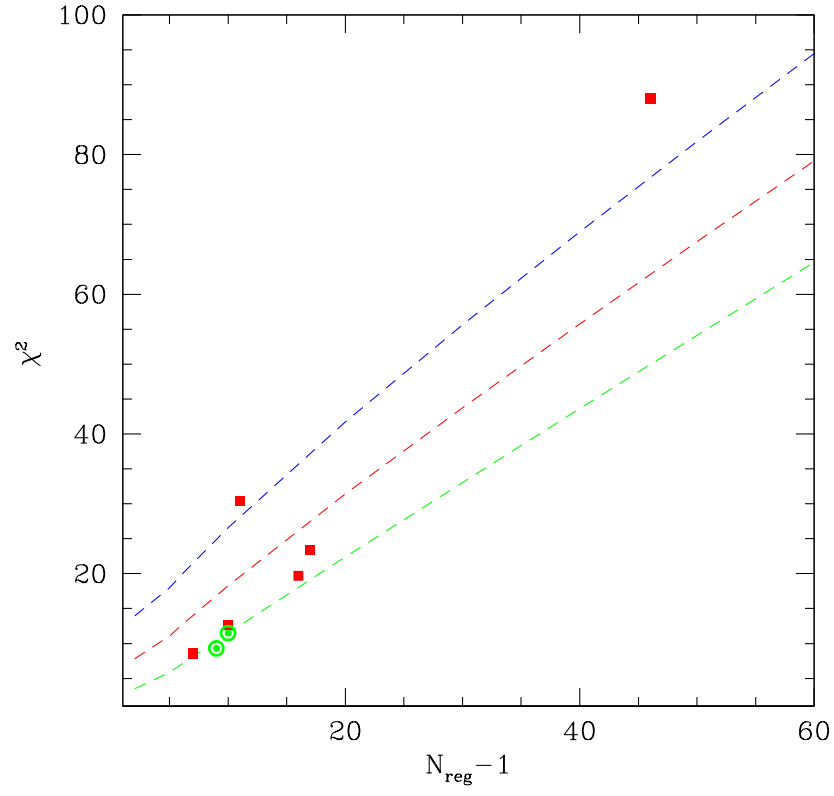


FIG. 17.— Red squares shows the χ^2 values versus the degrees of freedom (equal to $N_{\text{reg}} - 1$) for merger clusters, while circled green points shows the two relaxed clusters. Dashed lines shows the χ^2 values as a function of the degrees of freedom corresponding to 1, 2 and 3 σ confidence levels, from the lowest to the highest.

REFERENCES

- Abell, G. O., Corwin, Jr., H. G., & Olowin, R. P. 1989, *ApJS*, 70, 1
- Allen, S. W., Evrard, A. E., & Mantz, A. B. 2011, *ARA&A*, 49, 409
- Arnaud, K. A. 1996, in *Astronomical Society of the Pacific Conference Series*, Vol. 101, *Astronomical Data Analysis Software and Systems V*, ed. G. H. Jacoby & J. Barnes, 17–+
- Asplund, M., Grevesse, N., & Sauval, A. J. 2005, in *Astronomical Society of the Pacific Conference Series*, Vol. 336, *Cosmic Abundances as Records of Stellar Evolution and Nucleosynthesis*, ed. T. G. Barnes III & F. N. Bash, 25
- Barrena, R., Bosch, W., Girardi, M., & Spolaor, M. 2007, *A&A*, 469, 861
- Biffi, V., Dolag, K., & Böhringer, H. 2013, *MNRAS*, 428, 1395
- Bliton, M., Rizza, E., Burns, J. O., Owen, F. N., & Ledlow, M. J. 1998, *MNRAS*, 301, 609
- Brüggen, M., van Weeren, R. J., & Röttgering, H. J. A. 2012, *MNRAS*, 425, L76
- Canning, R. E. A. et al. 2012, *MNRAS*, 420, 2956
- Cash, W. 1979, *ApJ*, 228, 939
- Cassano, R. et al. 2013, *ApJ*, 777, 141
- Cuciti, V., Cassano, R., Brunetti, G., Dallacasa, D., Kale, R., Ettori, S., & Venturi, T. 2015, *A&A*, 580, A97
- Diaferio, A. 1999, *MNRAS*, 309, 610
- Diaferio, A., Geller, M. J., & Rines, K. J. 2005, *ApJ*, 628, L97
- Dupke, R. A., & Bregman, J. N. 2001a, *ApJ*, 562, 266
- . 2001b, *ApJ*, 547, 705
- . 2005, *ApJS*, 161, 224
- . 2006, *ApJ*, 639, 781
- Dupke, R. A., Mirabal, N., Bregman, J. N., & Evrard, A. E. 2007, *ApJ*, 668, 781
- Forman, W., Bechtold, J., Blair, W., Giacconi, R., van Speybroeck, L., & Jones, C. 1981, *ApJ*, 243, L133
- Giovannini, G., Bonafede, A., Feretti, L., Govoni, F., Murgia, M., Ferrari, F., & Monti, G. 2009, *A&A*, 507, 1257
- Giovannini, G., Tordi, M., & Feretti, L. 1999, *Nature*, 4, 141
- Girardi, M. et al. 2014, *A&A*, 565, A115
- Girardi, M., Barrena, R., Bosch, W., & Ellingson, E. 2008, *A&A*, 491, 379
- Govoni, F., Feretti, L., Giovannini, G., Böhringer, H., Reiprich, T. H., & Murgia, M. 2001, *A&A*, 376, 803
- Gutierrez, K., & Krawczynski, H. 2005, *ApJ*, 619, 161
- Henry, J. P., & Briel, U. G. 1996, *The Astrophysical Journal*, 472, 137
- Hiroi, K. et al. 2013, *ApJS*, 207, 36
- Kaastra, J. 1992, *An X-Ray Spectral Code for Optically Thin Plasmas* (Internal SRONLeiden Report, updated version 2.0)
- Kalberla, P. M. W., Burton, W. B., Hartmann, D., Arnal, E. M., Bajaja, E., Morras, R., & Pöppel, W. G. L. 2005, *A&A*, 440, 775
- Kempner, J. C., & Sarazin, C. L. 2001, *ApJ*, 548, 639
- Kempner, J. C., Sarazin, C. L., & Markevitch, M. 2003, *The Astrophysical Journal*, 593, 291
- Komatsu, E. et al. 2011, *ApJS*, 192, 18
- Liedahl, D. A., Osterheld, A. L., & Goldstein, W. H. 1995, *ApJ*, 438, L115
- Liu, A., Yu, H., Tozzi, P., & Zhu, Z.-H. 2015, *ApJ*, 809, 27
- Lyons, L. 2008, *Ann. Appl. Stat.*, 2, 887
- Mahdavi, A., Hoekstra, H., Babul, A., Balam, D. D., & Capak, P. L. 2007, *ApJ*, 668, 806
- Mann, A. W., & Ebeling, H. 2012, *MNRAS*, 420, 2120
- Markevitch, M., Gonzalez, A. H., David, L., Vikhlinin, A., Murray, S., Forman, W., Jones, C., & Tucker, W. 2002, *ApJ*, 567, L27
- Markevitch, M., Govoni, F., Brunetti, G., & Jerius, D. 2005a, *ApJ*, 627, 733
- . 2005b, *ApJ*, 627, 733
- Markevitch, M. et al. 2000, *The Astrophysical Journal*, 541, 542
- Mazzotta, P., Rasia, E., Moscardini, L., & Tormen, G. 2004, *MNRAS*, 354, 10
- Mewe, R., Gronenschild, E. H. B. M., & van den Oord, G. H. J. 1985, *A&AS*, 62, 197
- Mewe, R., Lemen, J. R., & van den Oord, G. H. J. 1986, *A&AS*, 65, 511
- Mitchell, R. J., Culhane, J. L., Davison, P. J. N., & Ives, J. C. 1976, *MNRAS*, 175, 29P
- Muriel, H., & Coenda, V. 2014, *A&A*, 564, A85
- Nagai, D., Kravtsov, A. V., & Kosowsky, A. 2003, *ApJ*, 587, 524
- Nagai, D., Lau, E. T., Avestruz, C., Nelson, K., & Rudd, D. H. 2013, *ApJ*, 777, 137
- Nelson, K., Lau, E. T., Nagai, D., Rudd, D. H., & Yu, L. 2014, *ApJ*, 782, 107
- Nousek, J. A., & Shue, D. R. 1989, *ApJ*, 342, 1207
- Oegerle, W. R., Hill, J. M., & Fitchett, M. J. 1995, *AJ*, 110, 32
- Ogrean, G. A., Brüggen, M., van Weeren, R. J., Röttgering, H., Croston, J. H., & Hoeft, M. 2013, *MNRAS*, 433, 812
- Ota, N., & Yoshida, H. 2015, *ArXiv e-prints*
- Owers, M. S. et al. 2014, *ApJ*, 780, 163
- Parekh, V., van der Heyden, K., Ferrari, C., Angus, G., & Holwerda, B. 2015, *A&A*, 575, A127
- Piffaretti, R., Arnaud, M., Pratt, G. W., Pointecouteau, E., & Melin, J.-B. 2011, *A&A*, 534, A109
- Pinto, C. et al. 2015, *A&A*, 575, A38
- Proust, D., Cuevas, H., Capelato, H. V., Sodré, Jr., L., Tomé Lehidey, B., Le Fèvre, O., & Mazure, A. 2000, *A&A*, 355, 443
- Rosati, P. et al. 2004, *AJ*, 127, 230
- . 2009, *A&A*, 508, 583
- Russell, H. R., Sanders, J. S., Fabian, A. C., Baum, S. A., Donahue, M., Edge, A. C., McNamara, B. R., & O’Dea, C. P. 2010, *MNRAS*, 406, 1721
- Russell, H. R. et al. 2011, *MNRAS*, 417, L1
- Sanders, J. S. 2006, *MNRAS*, 371, 829
- Sanders, J. S., Fabian, A. C., Smith, R. K., & Peterson, J. R. 2010, *MNRAS*, 402, L11
- Sato, K., Matsushita, K., Ishisaki, Y., Yamasaki, N. Y., Ishida, M., Sasaki, S., & Ohashi, T. 2008, *PASJ*, 60, 333
- Sato, T., Matsushita, K., Ota, N., Sato, K., Nakazawa, K., & Sarazin, C. L. 2011, *PASJ*, 63, 991
- Serra, A. L., & Diaferio, A. 2013, *ApJ*, 768, 116
- Shibata, R., Honda, H., Ishida, M., Ohashi, T., & Yamashita, K. 1999, *ApJ*, 524, 603
- Stanford, S. A. et al. 2005, *ApJ*, 634, L129
- Sugawara, C., Takizawa, M., & Nakazawa, K. 2009, *PASJ*, 61, 1293
- Takahashi, T., Mitsuda, K., Kelley, R., Fabian, A., Mushotzky, R., Ohashi, T., Petre, R., & on behalf of the ASTRO-H Science Working Group. 2014, *ArXiv e-prints*
- Tamura, T., Hayashida, K., Ueda, S., & Nagai, M. 2011, *PASJ*, 63, 1009
- Tamura, T. et al. 2014, *ApJ*, 782, 38
- Tozzi, P. et al. 2015, *ApJ*, 799, 93
- Tozzi, P., Santos, J. S., Nonino, M., Rosati, P., Borgani, S., Sartoris, B., Altieri, B., & Sanchez-Portal, M. 2013, *A&A*, 551, A45
- van Weeren, R. J., Brüggen, M., Röttgering, H. J. A., Hoeft, M., Nuza, S. E., & Intema, H. T. 2011, *A&A*, 533, A35
- van Weeren, R. J., Röttgering, H. J. A., Intema, H. T., Rudnick, L., Brüggen, M., Hoeft, M., & Oonk, J. B. R. 2012, *A&A*, 546, A124
- Wilms, J., Allen, A., & McCray, R. 2000, *ApJ*, 542, 914
- Yu, H., Serra, A. L., Diaferio, A., & Baldi, M. 2015, *ApJ*, 810, 37
- Yu, H., Tozzi, P., Borgani, S., Rosati, P., & Zhu, Z.-H. 2011, *A&A*, 529, A65
- Zhuravleva, I. et al. 2014, *Nature*, 515, 85

APPENDIX

SPECTRAL ANALYSIS RESULTS OF THE CLUSTERS

For each cluster analyzed in this work we report the best fit redshift z_X along with the statistical, systematic and total error in all the selected regions with reliable spectral fit.

TABLE 5

SPECTRAL ANALYSIS RESULTS OF ABELL 2142. COLUMN 1: REGION NUMBER; COLUMN 2: BEST-FIT REDSHIFT z_X OBTAINED FITTING THE 2.0-10 keV ENERGY RANGE; COLUMNS 3 & 4: LOWER AND UPPER 1σ ERROR BARS FROM FIT STATISTICS; COLUMNS 5 & 6: LOWER AND UPPER 1σ ERROR BARS FROM SYSTEMATICS ASSOCIATED TO THE ICM TEMPERATURE STRUCTURE; COLUMNS 7 & 8: TOTAL LOWER AND UPPER 1σ ERROR BARS COMPUTED AS

$$\sigma_{\text{tot}} = \sqrt{\sigma_{\text{stat}}^2 + \sigma_{\text{syst}}^2}.$$

| region | z | σ_{stat_b} | σ_{stat_u} | σ_{syst_b} | σ_{syst_u} | σ_{tot_b} | σ_{tot_u} |
|--------|--------|--------------------------|--------------------------|--------------------------|--------------------------|-------------------------|-------------------------|
| 0 | 0.0839 | -0.0030 | 0.0033 | -0.0009 | 0.0002 | -0.0031 | 0.0034 |
| 1 | 0.0847 | -0.0021 | 0.0026 | -0.0007 | 0.0013 | -0.0022 | 0.0029 |
| 2 | 0.0674 | -0.0048 | 0.0050 | -0.0014 | 0.0005 | -0.0051 | 0.0050 |
| 3 | 0.0881 | -0.0013 | 0.0029 | -0.0001 | 0.0018 | -0.0014 | 0.0034 |
| 4 | 0.0762 | -0.0064 | 0.0061 | -0.0040 | 0.0001 | -0.0076 | 0.0061 |
| 5 | 0.0863 | -0.0065 | 0.0058 | -0.0054 | 0.0026 | -0.0084 | 0.0063 |
| 6 | 0.0917 | -0.0022 | 0.0024 | -0.0001 | 0.0013 | -0.0022 | 0.0027 |
| 7 | 0.0866 | -0.0031 | 0.0032 | -0.0001 | 0.0015 | -0.0031 | 0.0035 |
| 8 | 0.0612 | -0.0064 | 0.0075 | -0.0001 | 0.0455 | -0.0064 | 0.0461 |
| 10 | 0.0808 | -0.0039 | 0.0039 | -0.0001 | 0.0040 | -0.0039 | 0.0055 |
| 11 | 0.0843 | -0.0030 | 0.0032 | -0.0001 | 0.0020 | -0.0030 | 0.0038 |
| 12 | 0.0885 | -0.0042 | 0.0098 | -0.0001 | 0.0010 | -0.0042 | 0.0099 |
| 13 | 0.0946 | -0.0034 | 0.0036 | -0.0001 | 0.0014 | -0.0034 | 0.0039 |
| 14 | 0.0787 | -0.0043 | 0.0036 | -0.0007 | 0.0013 | -0.0044 | 0.0039 |
| 15 | 0.0874 | -0.0043 | 0.0036 | -0.0001 | 0.0016 | -0.0043 | 0.0040 |
| 16 | 0.0860 | -0.0036 | 0.0038 | -0.0001 | 0.0030 | -0.0036 | 0.0049 |
| 17 | 0.0888 | -0.0029 | 0.0031 | -0.0020 | 0.0001 | -0.0035 | 0.0031 |
| 18 | 0.0908 | -0.0032 | 0.0024 | -0.0001 | 0.0013 | -0.0032 | 0.0027 |
| 20 | 0.0844 | -0.0029 | 0.0028 | -0.0004 | 0.0015 | -0.0030 | 0.0031 |
| 21 | 0.0885 | -0.0061 | 0.0083 | -0.0015 | 0.0025 | -0.0063 | 0.0087 |
| 22 | 0.0852 | -0.0033 | 0.0033 | -0.0012 | 0.0020 | -0.0036 | 0.0039 |
| 23 | 0.0841 | -0.0037 | 0.0038 | -0.0001 | 0.0020 | -0.0037 | 0.0043 |
| 25 | 0.0848 | -0.0028 | 0.0027 | -0.0001 | 0.0022 | -0.0028 | 0.0034 |
| 26 | 0.0811 | -0.0027 | 0.0029 | -0.0010 | 0.0010 | -0.0028 | 0.0031 |
| 27 | 0.0882 | -0.0040 | 0.0038 | -0.0010 | 0.0001 | -0.0041 | 0.0038 |
| 28 | 0.0831 | -0.0029 | 0.0024 | -0.0010 | 0.0001 | -0.0031 | 0.0024 |
| 29 | 0.0777 | -0.0044 | 0.0045 | -0.0017 | 0.0043 | -0.0047 | 0.0062 |
| 31 | 0.0914 | -0.0036 | 0.0040 | -0.0001 | 0.0025 | -0.0036 | 0.0047 |
| 32 | 0.0869 | -0.0023 | 0.0022 | -0.0010 | 0.0010 | -0.0025 | 0.0024 |
| 33 | 0.0878 | -0.0071 | 0.0100 | -0.0028 | 0.0132 | -0.0076 | 0.0166 |
| 34 | 0.0847 | -0.0027 | 0.0027 | -0.0007 | 0.0007 | -0.0028 | 0.0028 |
| 35 | 0.0966 | -0.0083 | 0.0058 | -0.0087 | 0.0043 | -0.0120 | 0.0072 |
| 36 | 0.0846 | -0.0027 | 0.0026 | -0.0006 | 0.0024 | -0.0028 | 0.0035 |
| 37 | 0.0821 | -0.0053 | 0.0050 | -0.0010 | 0.0060 | -0.0054 | 0.0078 |
| 38 | 0.0808 | -0.0045 | 0.0046 | -0.0013 | 0.0032 | -0.0047 | 0.0056 |
| 39 | 0.0853 | -0.0034 | 0.0035 | -0.0001 | 0.0016 | -0.0034 | 0.0038 |
| 40 | 0.0832 | -0.0033 | 0.0035 | -0.0007 | 0.0023 | -0.0034 | 0.0042 |
| 41 | 0.0826 | -0.0055 | 0.0041 | -0.0001 | 0.0034 | -0.0055 | 0.0053 |
| 42 | 0.0876 | -0.0024 | 0.0027 | -0.0001 | 0.0030 | -0.0024 | 0.0040 |
| 43 | 0.0820 | -0.0049 | 0.0053 | -0.0001 | 0.0050 | -0.0049 | 0.0073 |
| 44 | 0.0848 | -0.0027 | 0.0023 | -0.0008 | 0.0012 | -0.0028 | 0.0026 |
| 45 | 0.0884 | -0.0054 | 0.0051 | -0.0024 | 0.0036 | -0.0059 | 0.0062 |
| 47 | 0.0823 | -0.0037 | 0.0036 | -0.0001 | 0.0010 | -0.0037 | 0.0037 |
| 48 | 0.0885 | -0.0029 | 0.0031 | -0.0001 | 0.0010 | -0.0029 | 0.0033 |
| 49 | 0.0866 | -0.0028 | 0.0030 | -0.0001 | 0.0014 | -0.0028 | 0.0033 |
| 50 | 0.1124 | -0.0052 | 0.0063 | -0.0025 | 0.0045 | -0.0057 | 0.0077 |
| 51 | 0.0881 | -0.0049 | 0.0044 | -0.0001 | 0.0052 | -0.0049 | 0.0068 |

TABLE 6

SPECTRAL ANALYSIS RESULTS OF ABELL 2034. THE COLUMNS ARE THE SAME AS IN TABLE 5.

| region | z | σ_{stat_b} | σ_{stat_u} | σ_{syst_b} | σ_{syst_u} | σ_{tot_b} | σ_{tot_u} |
|--------|--------|--------------------------|--------------------------|--------------------------|--------------------------|-------------------------|-------------------------|
| 0 | 0.1056 | -0.0057 | 0.0056 | -0.0001 | 0.0033 | -0.0057 | 0.0065 |
| 1 | 0.1085 | -0.006 | 0.0068 | -0.0016 | 0.0014 | -0.0062 | 0.0069 |
| 2 | 0.1004 | -0.0062 | 0.0088 | -0.0001 | 0.0054 | -0.0062 | 0.0103 |
| 3 | 0.1089 | -0.0074 | 0.008 | -0.0017 | 0.0053 | -0.0075 | 0.0095 |
| 4 | 0.1318 | -0.0093 | 0.0076 | -0.0035 | 0.0001 | -0.0099 | 0.0076 |
| 6 | 0.1116 | -0.0038 | 0.0055 | -0.0001 | 0.0018 | -0.0038 | 0.0057 |
| 9 | 0.1301 | -0.0067 | 0.0058 | -0.0049 | 0.0001 | -0.0083 | 0.0058 |
| 10 | 0.1124 | -0.0055 | 0.0059 | -0.0018 | 0.0001 | -0.0057 | 0.0059 |
| 11 | 0.1099 | -0.0077 | 0.0061 | -0.0051 | 0.0001 | -0.0092 | 0.0061 |
| 12 | 0.1142 | -0.0075 | 0.0102 | -0.0035 | 0.0018 | -0.0082 | 0.0103 |
| 13 | 0.1011 | -0.0068 | 0.0095 | -0.0001 | 0.0040 | -0.0068 | 0.0103 |

TABLE 7
SPECTRAL ANALYSIS RESULTS OF ABELL 115. THE COLUMNS ARE THE SAME AS IN TABLE 5.

| region | z | σ_{stat_b} | σ_{stat_u} | σ_{syst_b} | σ_{syst_u} | σ_{tot_b} | σ_{tot_u} |
|--------|--------|--------------------------|--------------------------|--------------------------|--------------------------|-------------------------|-------------------------|
| 0 | 0.1980 | -0.0019 | 0.0036 | -0.0000 | 0.0025 | -0.0019 | 0.0044 |
| 1 | 0.1998 | -0.0027 | 0.0028 | -0.0000 | 0.0002 | -0.0027 | 0.0028 |
| 2 | 0.2026 | -0.0036 | 0.0039 | -0.0000 | 0.0037 | -0.0036 | 0.0053 |
| 4 | 0.1988 | -0.0051 | 0.0042 | -0.0000 | 0.0061 | -0.0051 | 0.0074 |
| 6 | 0.1922 | -0.0067 | 0.0083 | -0.0032 | 0.0018 | -0.0074 | 0.0085 |
| 8 | 0.1897 | -0.0124 | 0.0123 | -0.0037 | 0.0053 | -0.0129 | 0.0134 |
| 10 | 0.2090 | -0.0082 | 0.0086 | -0.0040 | 0.0040 | -0.0091 | 0.0095 |
| 11 | 0.2367 | -0.0060 | 0.0048 | -0.0087 | 0.0000 | -0.0106 | 0.0048 |
| 12 | 0.1679 | -0.0094 | 0.0113 | -0.0049 | 0.0020 | -0.0106 | 0.0115 |
| 14 | 0.1591 | -0.0064 | 0.0094 | -0.0000 | 0.0210 | -0.0064 | 0.0230 |
| 15 | 0.2263 | -0.0177 | 0.0107 | -0.0000 | 0.0000 | -0.0177 | 0.0107 |
| 17 | 0.1943 | -0.0069 | 0.0074 | -0.0038 | 0.0107 | -0.0079 | 0.0130 |

TABLE 8
SPECTRAL ANALYSIS RESULTS OF ABELL 520. THE COLUMNS ARE THE SAME AS IN TABLE 5.

| region | z | σ_{stat_b} | σ_{stat_u} | σ_{syst_b} | σ_{syst_u} | σ_{tot_b} | σ_{tot_u} |
|--------|--------|--------------------------|--------------------------|--------------------------|--------------------------|-------------------------|-------------------------|
| 0 | 0.2102 | -0.0037 | 0.0065 | -0.0001 | 0.0021 | -0.0037 | 0.0068 |
| 1 | 0.2069 | -0.0047 | 0.0043 | -0.0001 | 0.0027 | -0.0047 | 0.0050 |
| 2 | 0.1933 | -0.0085 | 0.0096 | -0.0001 | 0.0074 | -0.0085 | 0.0121 |
| 3 | 0.1962 | -0.0075 | 0.0076 | -0.0001 | 0.0024 | -0.0075 | 0.0079 |
| 5 | 0.2276 | -0.0155 | 0.0147 | -0.0025 | 0.0049 | -0.0157 | 0.0154 |
| 6 | 0.2207 | -0.0146 | 0.0079 | -0.0122 | 0.0001 | -0.0190 | 0.0079 |
| 8 | 0.1937 | -0.0128 | 0.0133 | -0.0018 | 0.0056 | -0.0129 | 0.0144 |
| 9 | 0.2048 | -0.0087 | 0.0075 | -0.0006 | 0.0027 | -0.0087 | 0.0079 |
| 10 | 0.2271 | -0.0164 | 0.0138 | -0.0039 | 0.0001 | -0.0168 | 0.0138 |
| 11 | 0.2152 | -0.0106 | 0.0096 | -0.0012 | 0.0058 | -0.0106 | 0.0112 |
| 12 | 0.2138 | -0.0046 | 0.0053 | -0.0001 | 0.0044 | -0.0046 | 0.0068 |
| 13 | 0.2282 | -0.0149 | 0.0126 | -0.0175 | 0.0006 | -0.0229 | 0.0126 |
| 14 | 0.2217 | -0.0153 | 0.0166 | -0.0066 | 0.0001 | -0.0166 | 0.0166 |
| 15 | 0.1921 | -0.0088 | 0.0085 | -0.0083 | 0.0001 | -0.0120 | 0.0085 |
| 16 | 0.195 | -0.0124 | 0.0131 | -0.0081 | 0.0001 | -0.0148 | 0.0131 |
| 17 | 0.1837 | -0.0085 | 0.0086 | -0.0001 | 0.0038 | -0.0085 | 0.0094 |
| 18 | 0.208 | -0.0102 | 0.0068 | -0.0057 | 0.0005 | -0.0116 | 0.0068 |
| 19 | 0.2104 | -0.0099 | 0.0093 | -0.0001 | 0.0114 | -0.0099 | 0.0147 |

TABLE 9
SPECTRAL ANALYSIS RESULTS OF 1RXSJ0603.3+4214. THE COLUMNS ARE THE SAME AS IN TABLE 5.

| region | z | σ_{stat_b} | σ_{stat_u} | σ_{syst_b} | σ_{syst_u} | σ_{tot_b} | σ_{tot_u} |
|--------|--------|--------------------------|--------------------------|--------------------------|--------------------------|-------------------------|-------------------------|
| 0 | 0.2317 | -0.0062 | 0.0065 | -0.0030 | 0.0004 | -0.0068 | 0.0065 |
| 1 | 0.2206 | -0.0069 | 0.0072 | -0.0021 | 0.0065 | -0.0072 | 0.0097 |
| 2 | 0.2347 | -0.0075 | 0.0119 | -0.0008 | 0.0071 | -0.0075 | 0.0138 |
| 4 | 0.2493 | -0.0067 | 0.0091 | -0.0069 | 0.0001 | -0.0096 | 0.0091 |
| 5 | 0.2198 | -0.0070 | 0.0063 | -0.0045 | 0.0001 | -0.0083 | 0.0063 |
| 6 | 0.2254 | -0.0108 | 0.0078 | -0.0055 | 0.0001 | -0.0121 | 0.0078 |
| 7 | 0.2294 | -0.0094 | 0.0066 | -0.0044 | 0.0021 | -0.0103 | 0.0069 |
| 8 | 0.2316 | -0.0091 | 0.0075 | -0.0001 | 0.0042 | -0.0091 | 0.0085 |

TABLE 10
SPECTRAL ANALYSIS RESULTS OF ABELL 2146. THE COLUMNS ARE THE SAME AS IN TABLE 5.

| region | z | σ_{stat_b} | σ_{stat_u} | σ_{syst_b} | σ_{syst_u} | σ_{tot_b} | σ_{tot_u} |
|--------|--------|--------------------------|--------------------------|--------------------------|--------------------------|-------------------------|-------------------------|
| 0 | 0.2292 | -0.0045 | 0.00312787 | -0.0000 | 0.0000 | -0.0045 | 0.0031 |
| 1 | 0.2282 | -0.0035 | 0.00311993 | -0.0017 | 0.0018 | -0.0039 | 0.0036 |
| 2 | 0.2277 | -0.0038 | 0.00571345 | -0.0000 | 0.0083 | -0.0038 | 0.0100 |
| 3 | 0.2282 | -0.0051 | 0.0026654 | -0.0027 | 0.0000 | -0.0057 | 0.0027 |
| 4 | 0.2294 | -0.0037 | 0.00436681 | -0.0000 | 0.0036 | -0.0037 | 0.0057 |
| 5 | 0.2276 | -0.0065 | 0.00615287 | -0.0001 | 0.0044 | -0.0065 | 0.0076 |
| 6 | 0.2325 | -0.0074 | 0.00676923 | -0.0055 | 0.0000 | -0.0092 | 0.0068 |
| 7 | 0.2354 | -0.0060 | 0.00619396 | -0.0114 | 0.0000 | -0.0129 | 0.0062 |
| 8 | 0.2473 | -0.0125 | 0.0069235 | -0.0223 | 0.0000 | -0.0255 | 0.0069 |
| 9 | 0.2436 | -0.0072 | 0.0066689 | -0.0036 | 0.0000 | -0.0080 | 0.0067 |
| 10 | 0.2277 | -0.0083 | 0.00881529 | -0.0000 | 0.0140 | -0.0083 | 0.0165 |
| 12 | 0.2372 | -0.0062 | 0.00682796 | -0.0010 | 0.0010 | -0.0063 | 0.0069 |
| 13 | 0.2326 | -0.0088 | 0.00909447 | -0.0025 | 0.0074 | -0.0091 | 0.0117 |
| 14 | 0.2256 | -0.0077 | 0.00950732 | -0.0025 | 0.0086 | -0.0081 | 0.0128 |
| 15 | 0.2495 | -0.0089 | 0.00691656 | -0.0015 | 0.0000 | -0.0090 | 0.0069 |
| 16 | 0.2226 | -0.0114 | 0.0110643 | -0.0060 | 0.0000 | -0.0129 | 0.0110 |
| 18 | 0.2505 | -0.0075 | 0.00798135 | -0.0080 | 0.0000 | -0.0110 | 0.0080 |

TABLE 11
SPECTRAL ANALYSIS RESULTS OF ABELL 1689. THE COLUMNS ARE THE SAME AS IN TABLE 5.

| region | z | σ_{stat_b} | σ_{stat_u} | σ_{syst_b} | σ_{syst_u} | σ_{tot_b} | σ_{tot_u} |
|--------|--------|--------------------------|--------------------------|--------------------------|--------------------------|-------------------------|-------------------------|
| 0 | 0.1767 | -0.0061 | 0.0048 | -0.0001 | 0.0037 | -0.0061 | 0.0060 |
| 1 | 0.1774 | -0.0047 | 0.0061 | -0.0014 | 0.0001 | -0.0049 | 0.0061 |
| 2 | 0.1864 | -0.0103 | 0.0109 | -0.0001 | 0.0066 | -0.0103 | 0.0127 |
| 3 | 0.1774 | -0.0065 | 0.0049 | -0.0019 | 0.002 | -0.0067 | 0.0052 |
| 4 | 0.1675 | -0.0074 | 0.0066 | -0.0019 | 0.0001 | -0.0076 | 0.0066 |
| 5 | 0.1859 | -0.0045 | 0.0038 | -0.0001 | 0.0016 | -0.0045 | 0.0041 |
| 6 | 0.1895 | -0.0084 | 0.0087 | -0.0001 | 0.0385 | -0.0084 | 0.0394 |
| 7 | 0.1859 | -0.006 | 0.0078 | -0.0001 | 0.0041 | -0.0060 | 0.0088 |
| 8 | 0.1826 | -0.0087 | 0.0073 | -0.0001 | 0.005 | -0.0087 | 0.0088 |
| 9 | 0.1847 | -0.0047 | 0.0071 | -0.0001 | 0.0031 | -0.0047 | 0.0077 |

TABLE 12
SPECTRAL ANALYSIS RESULTS OF ABELL 1835. THE COLUMNS ARE THE SAME AS IN TABLE 5.

| region | z | σ_{stat_b} | σ_{stat_u} | σ_{syst_b} | σ_{syst_u} | σ_{tot_b} | σ_{tot_u} |
|--------|--------|--------------------------|--------------------------|--------------------------|--------------------------|-------------------------|-------------------------|
| 0 | 0.2524 | -0.0031 | 0.0041 | -0.0024 | 0.0001 | -0.0039 | 0.0041 |
| 1 | 0.2547 | -0.0024 | 0.003 | -0.0001 | 0.0025 | -0.0024 | 0.0039 |
| 2 | 0.2478 | -0.003 | 0.0052 | -0.0001 | 0.0021 | -0.0030 | 0.0056 |
| 3 | 0.2474 | -0.003 | 0.0027 | -0.002 | 0.0003 | -0.0036 | 0.0027 |
| 4 | 0.2472 | -0.0048 | 0.006 | -0.002 | 0.0018 | -0.0052 | 0.0062 |
| 5 | 0.2408 | -0.0028 | 0.0045 | -0.0001 | 0.0052 | -0.0028 | 0.0068 |
| 6 | 0.2538 | -0.01 | 0.0065 | -0.0057 | 0.0016 | -0.0115 | 0.0066 |
| 7 | 0.2519 | -0.0046 | 0.0064 | -0.0028 | 0.0001 | -0.0053 | 0.0064 |
| 8 | 0.2486 | -0.006 | 0.0052 | -0.0001 | 0.0046 | -0.0060 | 0.0069 |
| 9 | 0.2372 | -0.0065 | 0.0073 | -0.0002 | 0.007 | -0.0065 | 0.0101 |
| 10 | 0.2496 | -0.0068 | 0.0078 | -0.0019 | 0.0023 | -0.0070 | 0.0081 |